Sex-specific Expression of Estradiol Derivatives, Hydropersulfides and Ether Lipids Regulates Ferroptosis Sensitivity of Kidney Tubules

Andreas Linkermann (✉ Andreas.Linkermann@ukdd.de)
University Hospital Carl Gustav Carus at the Technische Universität Dresden

Alexia Belavgeni
University Hospital Carl Gustav Carus at the Technische Universität Dresden https://orcid.org/0000-0001-6311-5858

Wulf Tonnus
University Hospital Carl Gustav Carus at the Technische Universität Dresden

Francesca Maremonti
University Hospital Carl Gustav Carus at the Technische Universität Dresden

Sider Penkov
TU Dresden

Melodie Mallais
University of Ottawa

Christine Gaillet
Institut Curie

Anne Brucker
University Hospital Carl Gustav Carus at the Technische Universität Dresden

Danny Schilling
University of Heidelberg

Lisa Schlicker
German Cancer Research Center

Nina Himmerkus
Christian-Albrechts-University https://orcid.org/0000-0002-2910-6728

Shubhangi Gavali
University Hospital Carl Gustav Carus at the Technische Universität Dresden https://orcid.org/0000-0003-2876-1453

Marlena Schlecht
University Hospital Carl Gustav Carus at the Technische Universität Dresden https://orcid.org/0000-0001-8893-5326

Karolin Flade

University Hospital Carl Gustav Carus at the Technische Universität Dresden https://orcid.org/0009-0009-5449-2825

Jorunn Becker
University Hospital Carl Gustav Carus at the Technische Universität Dresden https://orcid.org/0009-0004-5273-1320

Mirela Tmava
University Hospital Carl Gustav Carus at the Technische Universität Dresden https://orcid.org/0009-0002-4116-3634

Anne Haag
TU Dresden

Christian Hugo
University Hospital Carl Gustav Carus at the Technische Universität Dresden

Almut Schulze
German Cancer Research Center (DKFZ) https://orcid.org/0000-0002-8199-6422

Bernd Plietker
TU Dresden https://orcid.org/0000-0001-8423-6173

Jan Becker
University of Cologne

Joel Weinberg
University of Michigan

Svenja Lorenz
Helmholtz Zentrum München

Bettina Proneth
Helmholtz Zentrum München https://orcid.org/0000-0002-4119-9437

Marcus Conrad
Helmholtz Munich

Raphaël Rodriguez
Institut Curie, CNRS https://orcid.org/0000-0001-7668-446X

Stefan Bornstein
University Hospital Carl Gustav Carus at the Technische Universität Dresden

Tobias Dick
German Cancer Research Center (DKFZ)

Derel Pratt
University of Ottawa https://orcid.org/0000-0002-7305-745X

Maria Fedorova
TU Dresden https://orcid.org/0000-0002-4692-3885

Biological Sciences - Article

Keywords: nephron loss, acute tubular necrosis, cell death propagation, ferroptosis, β- estradiol, hydropersulfides, ether lipids, GPX4

Posted Date: November 15th, 2023

DOI: https://doi.org/10.21203/rs.3.rs-3601108/v1

Additional Declarations: There is **NO** Competing Interest.

Sex-specific Expression of Estradiol Derivatives, Hydropersulfides and Ether Lipids Regulates Ferroptosis Sensitivity of Kidney Tubules

Alexia Belavgeni[1], Wulf Tonnus[1], Francesca Maremonti[1], Sider Penkov[2], Melodie Mallais[3], Christine Gaillet[4], Anne Brucker[1], Danny Schilling[5,6], Lisa Schlicker[7], Nina Himmerkus[8], Shubhangi Gavali[1], Marlena Nastassja Schlecht[1], Karolin Flade[1], Jorunn Naila Becker[1], Mirela Tmava[1], Anne Haag[9], Christian Hugo[1], Almut Schulze[7], Bernd Plietker[9], Jan Ulrich Becker[10], Joel M. Weinberg[11], Svenja Lorenz[12], Bettina Proneth[12], Marcus Conrad[12], Raphaël Rodriguez[4], Stefan R. Bornstein[13-17], Tobias P. Dick[5,6], Derek A. Pratt[3], Maria Fedorova[2] and Andreas Linkermann[1, 18]

[1]Division of Nephrology, Department of Internal Medicine 3, University Hospital Carl Gustav Carus at the Technische Universität Dresden, Germany
[2]Center of Membrane Biochemistry and Lipid Research, University Hospital and Faculty of Medicine Carl Gustav Carus, Technische Universität Dresden
[3]Department of Chemistry and Biomolecular Sciences, University of Ottawa, Ottawa ON K1N 6N5, Canada
[4]Equipe Labellisée Ligue Contre le Cancer, Institut Curie, CNRS, INSERM, PSL Research University, Paris, France
[5]Division of Redox Regulation, German Cancer Research Center (DKFZ), DKFZ-ZMBH Alliance, Heidelberg, Germany
[6]Faculty of Biosciences, Heidelberg University, Heidelberg, Germany
[7]Division of Tumor Metabolism and Microenvironment, German Cancer Research Center (DKFZ), Heidelberg, Germany
[8]Institute of Physiology, Christian-Albrecht-University Kiel, Hermann-Rodewald-Str. 5, 24118 Kiel, Germany
[9]Chair of Organic Chemistry, Technische Universität Dresden, Dresden, Germany
[10]Institute of Pathology, University Hospital of Cologne, Cologne, Germany
[11]Division for Nephrology, University of Michigan Medical Center, Ann Arbor, MI, USA
[12]Institute of Metabolism and Cell Death, Helmholtz Zentrum München, Neuherberg, Germany
[13]Department of Internal Medicine 3, University Hospital Carl Gustav Carus at the Technische Universität Dresden, Dresden, Germany
[14]Diabetes and Nutritional Sciences, King's College London, London, UK.
[15]Center for Regenerative Therapies, Technische Universität Dresden, Dresden, Germany
[16]Paul Langerhans Institute Dresden of Helmholtz Centre Munich at University Clinic Carl Gustav Carus of TU Dresden Faculty of Medicine, Dresden, Germany
[17]Lee Kong Chian School of Medicine, Nanyang Technological University, Singapore, Singapore
[18]Division of Nephrology, Department of Medicine, Albert Einstein College of Medicine, Bronx, NY, USA

Word count 1.849

[#]**Correspondence:**
Andreas Linkermann, M.D., FASN
Division of Nephrology, Department of Internal Medicine III
University Hospital Carl Gustav Carus at the Technical University Dresden
Fetscherstrasse 74, 01307, Dresden, Germany
phone: +49-351-458-7681
fax: +49-531-458-5333
andreas.linkermann@ukdd.de
www.nephrology-dresden.org

Keywords: **nephron loss, acute tubular necrosis, cell death propagation, ferroptosis, β-estradiol, hydropersulfides, ether lipids, GPX4**

Abstract

Acute kidney tubular necrosis (ATN) mediates acute kidney injury (AKI) and nephron loss, the major risk factor for chronic kidney disease (CKD) progression and end-stage renal disease (ESRD)[1-3]. For decades, it has been known that female tissue is less sensitive to AKI[4,5], but the underlying mechanisms have remained elusive. As a specific feature, ATN is characterized by dynamic cell death propagation along the tubular compartment, mediated by ferroptosis in male mice[6,7]. Herein we demonstrate that ferroptotic cell death propagation is abrogated in female kidney tubules. Ferroptosis sensitivity in females was decreased by estradiol and its derivatives, which function as radical-trapping antioxidants (RTAs). Female sex-specific tubular expression of ferroptosis suppressor protein 1 (FSP1, also AIFM2) functions to regenerate the estradiol derivatives from their oxidation products, thereby potentiating RTA capacity. In addition, females exhibited much higher levels of anti-ferroptotic hydropersulfides detected directly from the most sensitive tubular compartment. In contrast, male proximal tubules express alkylglycerone phosphate synthase (AGPS) and fatty acyl-CoA reductase 1 (FAR1), key enzymes required for the generation of ether lipids which sensitize to ferroptosis. In summary, we uncover three independent mechanisms that collectively explain higher ferroptosis sensitivity of male over female tubular tissue and may function as therapeutic targets.

Recently, a broad review of 5.4 million Medicare recipients demonstrated a significantly lower AKI incidence in women[8]. Similarly, numerous clinical investigations have revealed a higher incidence of AKI and higher AKI-associated mortality for the male sex[9-13]. We hypothesized that such sex differences relate to sensitivity to acute tubular necrosis, a hallmark of which is cell death by ferroptosis, a form of iron-catalysed necrosis and the predominant type of cell

death in renal tubules in AKI[7,14,15]. We therefore isolated renal tubules from male and female mice and compared spontaneous cell death propagation (**Figure 1a, Figure S1a and Video S1**). When tubules with higher than 90% SYTOX positivity were counted (**Figure S1b**), cell death spread in male tubules as expected from previous work[7,15], but cell death propagation was abrogated in female tubules (**Figure 1b**). In line with this observation, LDH released over time was significantly lower from the tubules of female mice (**Figure 1c**). While the lipophilic ferroptosis inhibitor ferrostatin-1 (Fer-1) reduced LDH release in male tubules, it had no effect on female tubules (**Figures 1d-e**). As a control, combined necroptosis- and pyroptosis-deficient kidney tubules isolated from mixed lineage kinase domain-like (MLKL) and gasdermin D (GSDMD) double knockout mice were assessed with no significant difference compared to wild type littermates (**Figure S1c**). While male mice are known to be protected from ischemia-reperfusion injury (IRI) by Fer-1[7], this small molecule at a concentration of 10 mg/kg body weight failed to protect female mice from increases in serum urea and serum creatinine concentrations and from structural damage (**Figure S1d-g**). Primary kidney tubular cells that grew out of isolated kidney tubules (**Figure S1h, Video S2**) were sensitive to ferroptosis induction by the GPX4 inhibitor RSL3, FINO2 and ferroptocide (FTC), but no differences were observed between male and female cells (**Figure S1i-n**). In the same assay, erastin, imidazole ketone erastin (IKE), FIN56 or treatment with TNFα and the pan caspase-inhibitor zVAD-fmk (TZ) failed to cause any LDH release, indicating that cell death propagation by ferroptosis relates to the existence of the tubular structure. We therefore set out to investigate cell death propagation in more detail in male tubules (**Video S3**). We detected an accompanying calcium signal that overlayed with SYTOX-positivity (**Figure S2a-b, Video S4**) and was preceded by disappearance of mitotracker (**Figure S2c, Video S5**). Electron microscopy revealed that mitochondria were damaged in the transition zone of tubules undergoing necrosis and were

prominently ballooned in the SYTOX-positive necrotic part (**Figures S2d-f**). Collectively, these data indicate that ferroptotic cell death propagation is abrogated in female kidney tubules. *Gpx4*$^{fl/fl}$;*ROSA26-CreER*^{T2} transgenic mice have been recently demonstrated to succumb from tubular necrosis within 14 days following activation of the Cre recombinase[16]. While there was no significant difference in overall survival between sexes (**Figure S3a**), less tubular necrosis was detected in females alongside with lower serum concentrations of creatinine and urea (**Figure S3b-f**) 10 days following tamoxifen application in these mice. These data are in line with a previous report[17] and indicated that females were less sensitive to ATN and AKI in a ferroptosis-specific system.

We next investigated how sex hormones affect ferroptotic cell death. In ferroptosis-sensitive cell lines (HT1080 cells, NIH-3T3 cells), simultaneous treatment with either 17β-estradiol or its hydroxylated derivative 2-hydroxyestradiol (2OH-E2) protected from RSL3-induced ferroptosis (**Figure 2a-c**). In keeping with previously published cell culture assays[18], 17β-estradiol protected three ferroptosis-sensitive cell lines from ferroptosis induced by erastin, FIN56, FINO2 and FTC (**Figure S4**), while testosterone did not (**Figure S5**). Comparable effects were detected upon 16 h pre-treatment with the hormones (**Figure S6-7**). Using FENIX assays[19], we confirmed that 17β-estradiol, 2OH-E2 and 4OH-E2, but not cholesterol or testosterone, function as radical-trapping antioxidants (RTAs) (**Figure 2d-i**). Although catechol estrogens have been reported to possess antioxidant properties, the FENIX assays demonstrate and quantitate this in lipid bilayers which is key to making the connection to ferroptosis suppression. In addition to reacting as an RTA, we found that 4OH-E2 can function as an iron chelator while 2OH-E2 does not (**Figure S8**). We therefore hypothesized that the catechol moiety in 2OH-E2 mediates its potent RTA activity and generated a more simplified dihydrobenzene structure (5,6,7,8-tetrahydronaphthalene-2,3-diol). This compound exhibited anti-ferroptotic potency comparable to the estradiol metabolites (**Figure S9**). We concluded

that the catechol mediates the anti-ferroptotic effect. Indeed, 2OH-E2 protected male tubules from LDH release (**Figure 2j**) at least as pronounced as Fer-1 (**Figure 1d**). This can be rationalized based on the similar potencies kinetics with which 2OH-E2 (k_{inh} = 1.0 ± 0.1 × 10^4 M^{-1} s^{-1}) and Fer-1 (k_{inh} = 8.2 ± 0.3 × 10^4 M^{-1} s^{-1}) react with propagating lipidperoxyl radicals in phospholipid bilayers[20]. In a mouse model of kidney ischemia-reperfusion injury (IRI), 2OH-E2 prevented renal damage (**Figure 2k-l**) and resulted in significantly lower serum concentrations of serum creatinine and serum urea (**Figure 2m-n**). Collectively, these data demonstrate that estradiol and particularly its hydroxylated derivatives function as ferroptosis inhibitors.

We wondered whether hydroxyestradiol derivatives, once having undergone oxidation to the corresponding quinones, can be regenerated as demonstrated for coenzyme Q10 and vitamin K[21]. The addition of recombinant FSP1 to the FENIX assays resulted in a potentiation of RTA activity among all estradiol derivatives tested (**Figures 3a-c**). We therefore propose an NADPH-dependent regenerative mechanism of estradiol regeneration (**Figure 3d, Figure S10a-f**). Similar effects were obtained in cell-free systems wherein ascorbate or superoxide thermal source-1 (SOTS-1) were tested for their capacity to regenerate estradiol derivatives (**Figure S10j-n**). When employing a publicly available database, we further noticed that proximal kidney tubules of female but not male mice express FSP1 mRNA (**Figure 3e**). In primary murine tubule lysates, FSP1 protein expression was higher in female than male tubules (**Figure 3f**), but absent in FSP1-deficient mice (**Figure S10o**). Unexpectedly, tubules isolated from FSP1-deficient female mice released similar LDH levels (**Figure 3g**) and were not supersensitive to kidney IRI (**Figure 3h and Figure S10p-r**) compared to wild type littermates, indicating a compensatory mechanism in this strain. Indeed, when we investigated the expression levels of the thioredoxin-reductase 1 (TXNRD1) pathway in lysates of renal tubules of these mice, we found upregulation of peroxiredoxin 1 (PRX1) (**Figure 3i**), while ACSL4

and GPX4 expression remained unaltered (**Figure S10s**). Upon inhibition of the PRX1 pathway (that also involves thioredoxin reductase 1) with FTC[22], we unleashed the hypersensitivity, detecting unusually high levels of LDH release from isolated tubules that was entirely reversed by the addition of Fer-1 (**Figure 3j**). These data indicate that FSP1 regenerates estradiol derivatives in the female proximal tubule to protect from ferroptosis and ATN.

Upon assessment of the protein expression levels of ferroptosis key regulating enzymes in male vs female tubular lysates, we observed an increase in cystathionine gamma-lyase (CSE) and a corresponding decrease in cystathionine beta-synthase (CBS) while ACSL4, GPX4 and p450 oxidoreductase (POR) were equally expressed. This pattern led us to hypothesize that anti-ferroptotic hydroper-/polysulfides[23] might additively protect female kidney tubules in an estradiol-independent manner (**Figure 4a-c**). We therefore extended our investigation to persulfide deoxygenase (ETHE1) and the sulfide-quinone oxidoreductase (SQR). While male tubules exhibited higher expression levels of ETHE1, the SQR expression was unchanged (**Figure 4d**). This indicated increased degradation of the hydropersulfide GSSH, a known suppressor of ferroptosis[23,24], in male tubules. We then compared relative levels of sulphur-containing metabolites between male and female tubules. We detected significantly higher levels of GSSH and hydrogen sulfide (H_2S) in female vs male tubules. H_2S_2 and CysSSH also showed a tendency toward higher levels in female kidney tubules while cysteine and GSH exhibited no differences (**Figure 4e-j**). Additionally, treatment of cells with hydrogen persulfide Na_2S_2 (a persulfide donor converting GSH to GSSH), resulted in protection of HT1080 cells from RSL3-induced ferroptosis, in contrast to the sulphide donor Na_2S (**Figure S11a-b**). These experiments suggested that female mice synthetize higher levels of anti-ferroptotic hydropersulfides in their kidney tubules.

In contrast to hydropersulfides, the plasticity of ether lipids has recently been demonstrated to sensitize to ferroptosis[25]. We therefore investigated the key enzymes in the ether lipid

production pathway, fatty acyl-CoA reductase 1 (FAR1) and alkylglycerone phosphate synthase (AGPS) (**Figure 5a**), in the tubular systems of both sexes. The mRNAs of these enzymes were expressed to a higher degree in male proximal tubules (**Figure 5b**). In contrast to male tubules, protein expression of both FAR1 and AGPS was absent in female tubules (**Figure 5c**). This led us to directly compare freshly isolated and necrotic male and female tubules by lipidomics. As demonstrated in **Figure 5d**, ether phospholipid abundance was higher at baseline and markedly elevated upon damage in male kidney tubules, while corresponding ester phospholipids did not exhibit this pattern (**Figure S12**). These data indicated that the pro-ferroptotic plasticity of ether lipids is increased in male but not female tubules.

In 1988, it was first observed that daily intraperitoneal injections of ferric nitrilotriacetate resulted in the death of all male mice within 6 days, whereas all female and castrated male mice survived 3 months of treatment[26]. In addition, ferroptosis-mediated effects following iron application recently indicated a role of iron in the damaging process of solid organs including the kidneys[27]. Here, we identified three independent mechanisms, all of which are sex specific and highlight a predominant role in ferroptosis propagation during ATN in male mice (**Figure S13**). While estradiols, regenerated by FSP1, and hydropersulfides protect female tubules, males are hypersensitive by increased plasticity to ether lipids. In conclusion, these delicate systems suggest ferroptosis targeting to be of particular benefit for male tubules. Ferroptosis sensitivity, therefore, might explain the higher susceptibility of males to AKI[8].

A limitation of our study relates to our tubule isolation protocol, representing an *ex vivo* model. However, cell death propagation was recently detected directly by longitudinal intravital imaging following IRI[28], confirming the cell death propagation pattern investigated here to occur in male mice *in situ* in a similar manner. Finally, our experiments indicate a role of

ferroptosis in solid organ transplantation, including the possibility to target ferroptosis for the purpose of prevention of cell death and necroinflammation[29], predominantly in male organs.

References

1 Kellum, J. A. *et al.* Acute kidney injury. *Nature reviews. Disease primers* **7**, 52, doi:10.1038/s41572-021-00284-z (2021).

2 Sharfuddin, A. A. & Molitoris, B. A. Pathophysiology of ischemic acute kidney injury. *Nature reviews. Nephrology* **7**, 189-200, doi:10.1038/nrneph.2011.16 (2011).

3 Venkatachalam, M. A., Weinberg, J. M., Kriz, W. & Bidani, A. K. Failed Tubule Recovery, AKI-CKD Transition, and Kidney Disease Progression. *Journal of the American Society of Nephrology : JASN* **26**, 1765-1776, doi:10.1681/asn.2015010006 (2015).

4 Park, K. M., Kim, J. I., Ahn, Y., Bonventre, A. J. & Bonventre, J. V. Testosterone is responsible for enhanced susceptibility of males to ischemic renal injury. *The Journal of biological chemistry* **279**, 52282-52292, doi:10.1074/jbc.M407629200 (2004).

5 Silbiger, S. R. & Neugarten, J. The impact of gender on the progression of chronic renal disease. *American journal of kidney diseases : the official journal of the National Kidney Foundation* **25**, 515-533, doi:10.1016/0272-6386(95)90119-1 (1995).

6 Belavgeni, A., Meyer, C., Stumpf, J., Hugo, C. & Linkermann, A. Ferroptosis and Necroptosis in the Kidney. *Cell chemical biology* **27**, 448-462, doi:10.1016/j.chembiol.2020.03.016 (2020).

7 Linkermann, A. *et al.* Synchronized renal tubular cell death involves ferroptosis. *Proceedings of the National Academy of Sciences of the United States of America* **111**, 16836-16841, doi:10.1073/pnas.1415518111 (2014).

8 Xue, J. L. *et al.* Incidence and mortality of acute renal failure in Medicare beneficiaries, 1992 to 2001. *Journal of the American Society of Nephrology : JASN* **17**, 1135-1142, doi:10.1681/asn.2005060668 (2006).

9 Bagshaw, S. M. *et al.* Prognosis for long-term survival and renal recovery in critically ill patients with severe acute renal failure: a population-based study. *Critical care (London, England)* **9**, R700-709, doi:10.1186/cc3879 (2005).

10 Chertow, G. M. *et al.* Predictors of mortality and the provision of dialysis in patients with acute tubular necrosis. The Auriculin Anaritide Acute Renal Failure Study Group. *Journal of the American Society of Nephrology : JASN* **9**, 692-698, doi:10.1681/asn.V94692 (1998).

11 Cosentino, F., Chaff, C. & Piedmonte, M. Risk factors influencing survival in ICU acute renal failure. *Nephrology, dialysis, transplantation : official publication of the European Dialysis and Transplant Association - European Renal Association* **9 Suppl 4**, 179-182 (1994).

12 Mehta, R. L., Pascual, M. T., Gruta, C. G., Zhuang, S. & Chertow, G. M. Refining predictive models in critically ill patients with acute renal failure. *Journal of the American Society of Nephrology : JASN* **13**, 1350-1357, doi:10.1097/01.asn.0000014692.19351.52 (2002).

13 Paganini, E. P., Halstenberg, W. K. & Goormastic, M. Risk modeling in acute renal failure requiring dialysis: the introduction of a new model. *Clinical nephrology* **46**, 206-211 (1996).

14 Maremonti, F., Meyer, C. & Linkermann, A. Mechanisms and Models of Kidney Tubular Necrosis and Nephron Loss. *Journal of the American Society of Nephrology : JASN*, doi:10.1681/asn.2021101293 (2022).

15 Tonnus, W. *et al.* Dysfunction of the key ferroptosis-surveilling systems hypersensitizes mice to tubular necrosis during acute kidney injury. *Nature communications* **12**, 4402, doi:10.1038/s41467-021-24712-6 (2021).
16 Friedmann Angeli, J. P. *et al.* Inactivation of the ferroptosis regulator Gpx4 triggers acute renal failure in mice. *Nature cell biology* **16**, 1180-1191, doi:10.1038/ncb3064 (2014).
17 Ide, S. *et al.* Sex differences in resilience to ferroptosis underlie sexual dimorphism in kidney injury and repair. *Cell reports* **41**, 111610, doi:10.1016/j.celrep.2022.111610 (2022).
18 Mishima, E. *et al.* Drugs Repurposed as Antiferroptosis Agents Suppress Organ Damage, Including AKI, by Functioning as Lipid Peroxyl Radical Scavengers. *Journal of the American Society of Nephrology : JASN*, doi:10.1681/asn.2019060570 (2019).
19 Shah, R., Farmer, L. A., Zilka, O., Van Kessel, A. T. M. & Pratt, D. A. Beyond DPPH: Use of Fluorescence-Enabled Inhibited Autoxidation to Predict Oxidative Cell Death Rescue. *Cell chemical biology* **26**, 1594-1607.e1597, doi:10.1016/j.chembiol.2019.09.007 (2019).
20 Poon, J. F., Zilka, O. & Pratt, D. A. Potent Ferroptosis Inhibitors Can Catalyze the Cross-Dismutation of Phospholipid-Derived Peroxyl Radicals and Hydroperoxyl Radicals. *Journal of the American Chemical Society* **142**, 14331-14342, doi:10.1021/jacs.0c06379 (2020).
21 Mishima, E. *et al.* A non-canonical vitamin K cycle is a potent ferroptosis suppressor. *Nature*, doi:10.1038/s41586-022-05022-3 (2022).
22 Llabani, E. *et al.* Diverse compounds from pleuromutilin lead to a thioredoxin inhibitor and inducer of ferroptosis. *Nature Chemistry*, doi:10.1038/s41557-019-0261-6 (2019).
23 Barayeu, U. *et al.* Hydropersulfides inhibit lipid peroxidation and ferroptosis by scavenging radicals. *Nature chemical biology* **19**, 28-37, doi:10.1038/s41589-022-01145-w (2023).
24 Wu, Z. *et al.* Hydropersulfides Inhibit Lipid Peroxidation and Protect Cells from Ferroptosis. *Journal of the American Chemical Society* **144**, 15825-15837, doi:10.1021/jacs.2c06804 (2022).
25 Zou, Y. *et al.* Plasticity of ether lipids promotes ferroptosis susceptibility and evasion. *Nature*, doi:10.1038/s41586-020-2732-8 (2020).
26 Li, J. L., Okada, S., Hamazaki, S., Deng, I. L. & Midorikawa, O. Sex differences in ferric nitrilotriacetate-induced lipid peroxidation and nephrotoxicity in mice. *Biochimica et biophysica acta* **963**, 82-87, doi:10.1016/0005-2760(88)90340-2 (1988).
27 Van Coillie, S. *et al.* Targeting ferroptosis protects against experimental (multi)organ dysfunction and death. *Nature communications* **13**, 1046, doi:10.1038/s41467-022-28718-6 (2022).
28 Bordoni, L. *et al.* Longitudinal tracking of acute kidney injury reveals injury propagation along the nephron. *Nature communications* **14**, 4407, doi:10.1038/s41467-023-40037-y (2023).
29 Sarhan, M., Land, W. G., Tonnus, W., Hugo, C. P. & Linkermann, A. Origin and Consequences of Necroinflammation. *Physiological reviews* **98**, 727-780, doi:10.1152/physrev.00041.2016 (2018).

30 von Mässenhausen, A. *et al.* Dexamethasone sensitizes to ferroptosis by glucocorticoid receptor-induced dipeptidase-1 expression and glutathione depletion. *Science advances* **8**, eabl8920, doi:10.1126/sciadv.abl8920 (2022).
31 Li, B. *et al.* Besting vitamin E: sidechain substitution is key to the reactivity of naphthyridinol antioxidants in lipid bilayers. *Journal of the American Chemical Society* **135**, 1394-1405, doi:10.1021/ja309153x (2013).
32 He, Y., Tang, J., Luo, M. & Zeng, X. Regioselective and Chemoselective Reduction of Naphthols Using Hydrosilane in Methanol: Synthesis of the 5,6,7,8-Tetrahydronaphthol Core. *Organic letters* **20**, 4159-4163, doi:10.1021/acs.orglett.8b01273 (2018).
33 MacLean, B. *et al.* Skyline: an open source document editor for creating and analyzing targeted proteomics experiments. *Bioinformatics (Oxford, England)* **26**, 966-968, doi:10.1093/bioinformatics/btq054 (2010).
34 Folch, J., Lees, M. & Sloane Stanley, G. H. A simple method for the isolation and purification of total lipides from animal tissues. *The Journal of biological chemistry* **226**, 497-509 (1957).
35 Lange, M. *et al.* AdipoAtlas: A reference lipidome for human white adipose tissue. *Cell reports. Medicine* **2**, 100407, doi:10.1016/j.xcrm.2021.100407 (2021).
36 Tonnus, W. *et al.* Gasdermin D-deficient mice are hypersensitive to acute kidney injury. *Cell death & disease* **13**, 792, doi:10.1038/s41419-022-05230-9 (2022).

Acknowledgements

We would like to cordially thank Anne Pioch, Romy Opitz and Monique Hoffmann for expert technical assistance. Work in the Linkermann Lab was funded by the German Research Foundation SFB-TRR205, SFB-TRR 127, SPP2306, and a Heisenberg-Professorship to A.L., project number 324141047, and the international research training group (IRTG) 2251. It was further supported by the BMBF (FERROPath consortium), the TU Dresden / Kings College London transcampus initiative and the DFG-Sachbeihilfe LI 2107/10-1. Work in the Conrad was supported by Deutsche Forschungsgemeinschaft (DFG) (CO 291/7-1, # 428858739 and the Priority Program SPP 2306 [CO 291/9-1, #461385412; CO 291/10-1, #461507177]) and PR 1752/3-1 to B.P., the BMBF program FERROPATH (01EJ2205B), and the European Research Council (ERC) under the European Union's Horizon 2020 research and innovation programme (grant agreement No. GA 884754) to M.C. D.A.P. and M.M. acknowledge the Natural Sciences and Engineering Research Council of Canada for their support (RGPIN-2022-05058). R.R. is supported by the European Research Council under the European Union's Horizon 2020 research and innovation programme (grant agreement no. 647973), Foundation Charles Defforey-Institut de France. Work in the Fedorova lab is supported by ''Sonderzuweisung zur Unterstützung profilbestimmender Struktureinheiten 2021'' by the SMWK, TG70 by Sächsische Aufbaubank and SMWK, the measure is co-financed with tax funds on the basis of the budget passed by the Saxon state parliament (to M.F.), Deutsche Forschungsgemeinschaft (FE 1236/5-1 to M.F.), and Bundesministerium für Bildung und Forschung (01EJ2205A, FERROPath to M.F.).

Author contributions

A.B, W.T., F.M., S.P., M.M., C.G., A.Br., D.S., L.S., N.H., S.G., M.S., K.F., J.N.B., M.T. and J.B. performed the experiments. B.P., M.C., R.R., D.A.P. and M.F. provided essential materials. C.H., A.S., J.M.W., M.M., D.A.P. and S.R.B. helped with the revision of the manuscript. A.B. and A.L. designed the study and analyzed all primary data. A.B. and A.L. wrote the manuscript.

Competing interests

All authors declare no conflict of interest regarding any of the presented data in this manuscript.

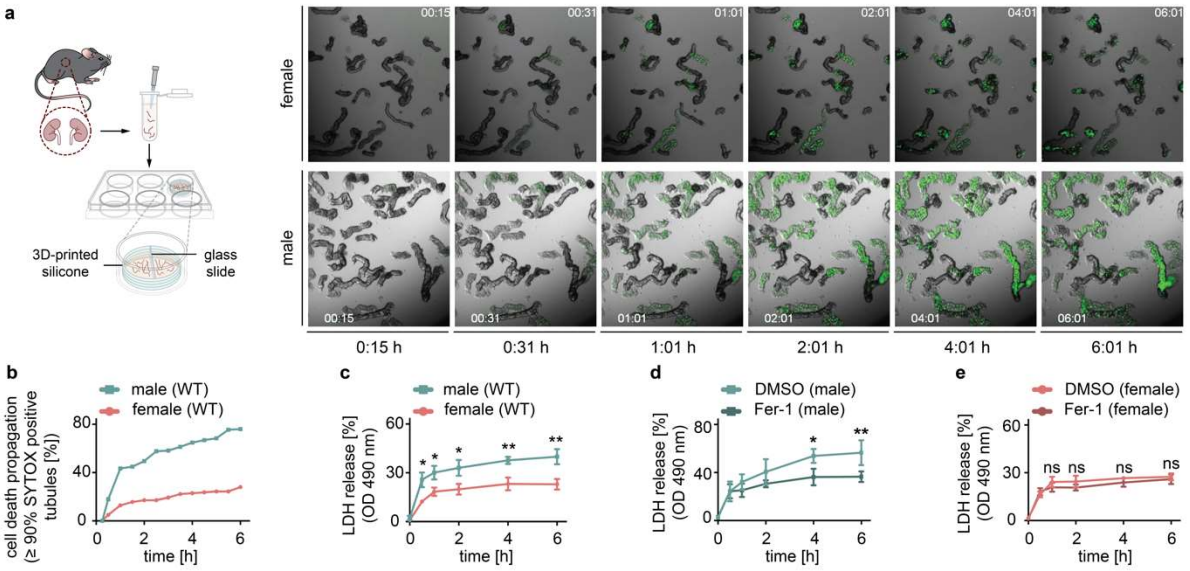

Figure 1. Abrogated ferroptotic cell death propagation in female kidney tubules. **a**, Schematic representation of the experimental setup followed for the simultaneous live imaging of tubules isolated from male and female mice. Representative images of the time lapse video of female and male tubules over time. Note the absence of the propagation of the SYTOX positive signal in female tubules. **b**, Tubular cell death propagation over time. **c**, LDH release of spontaneously dying tubules isolated from male (N = 3) and female (N = 3) wild type (WT) mice over time. **d**, Time course of LDH release of tubules isolated from WT male mice treated with vehicle (N = 7) or 30 µM Fer-1 (N = 3). **e**, Time course of LDH release of tubules isolated from WT female mice treated with vehicle (N = 3) or 30 µM Fer-1 (N = 3). Data presented as mean ± SD. **p* < 0.05; ***p* < 0.01; ns = non-significant.

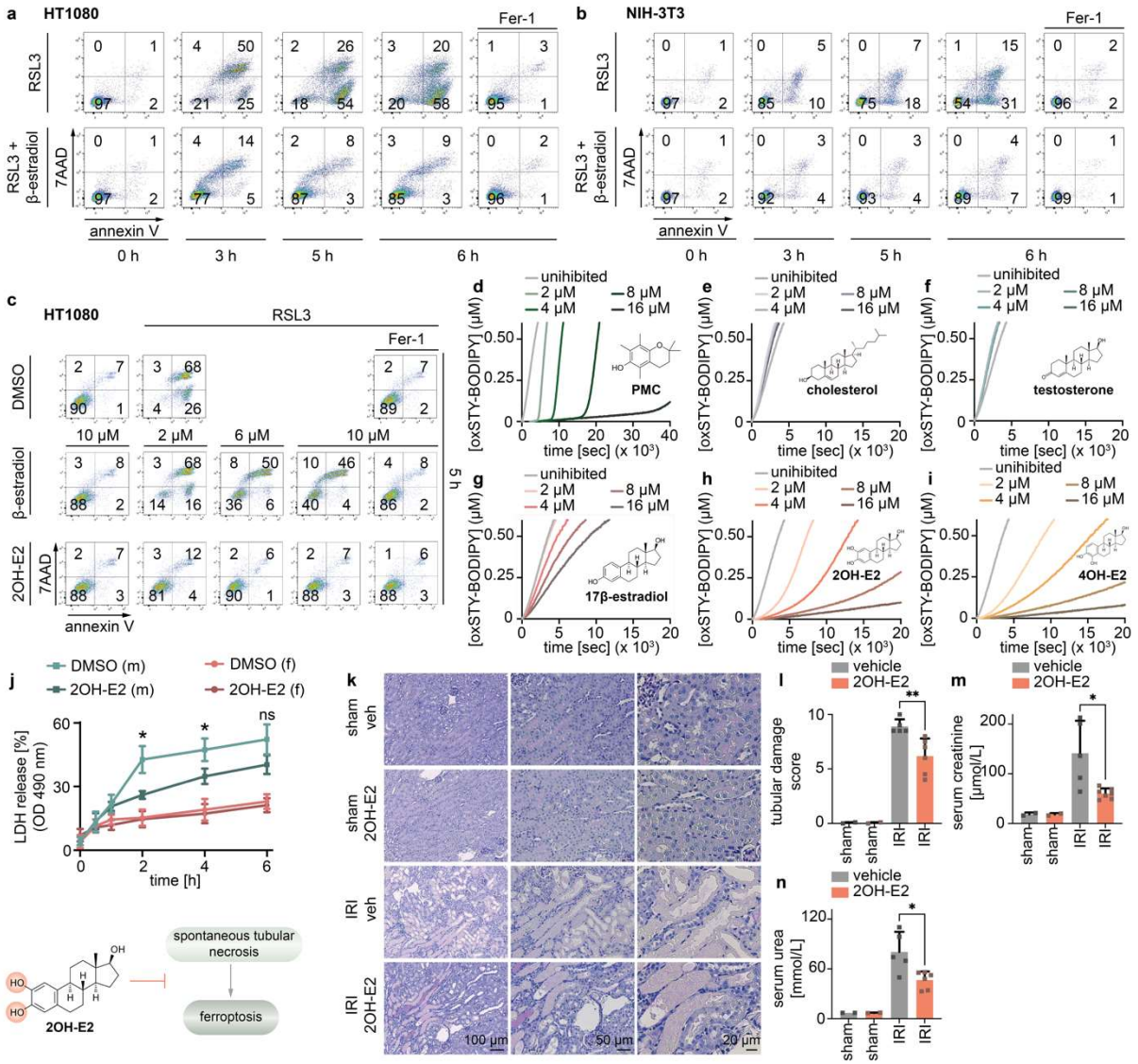

Figure 2. Estradiol derivatives function as radical trapping antioxidants and protect female kidney tubules from ferroptosis. **a**, Flow cytometry analysis of HT1080 and **b,** NIH-3T3 cells treated simultaneously with RSL3 (1.13 µM) and 17β-estradiol (10 µM) for indicated time points. Fer-1 (1 µM) serves as a protection control. Cells were stained with annexin V and 7AAD. **c,** Flow cytometry of HT1080 cells treated with RSL3 (1.13 µM) for 4 h and simultaneous treatment with indicated concentrations of 17β-estradiol or 2-hydroxyestradiol (2-OHE2). **d-i,** FENIX assay for different concentrations (2-16 µM) of PMC (2,7,8-pentamethyl-6-chromanol), cholesterol, testosterone, 17β-estradiol, 2OH-E2 and 4-hydroxyestradiol (4OH-E2). **j,** LDH release over time of freshly isolated tubules from male and female mice treated with vehicle control (N = 3) or 10 µM 2OH-E2 (N = 3). **k,** Representative micrographs of periodic acid-Schiff (PAS)-stained sections of sham- or IRI-operated male WT while treated with vehicle or 15 mg/kg 2OH-E2. **l,** Tubular damage score was quantified for the experiment presented in **k**. **m-n,** Serum levels of creatinine and urea of the WT male mice of the experiment presented in **k**. Data presented as mean ± SD. **p* < 0.05; ***p* < 0.01; ns = non-significant.

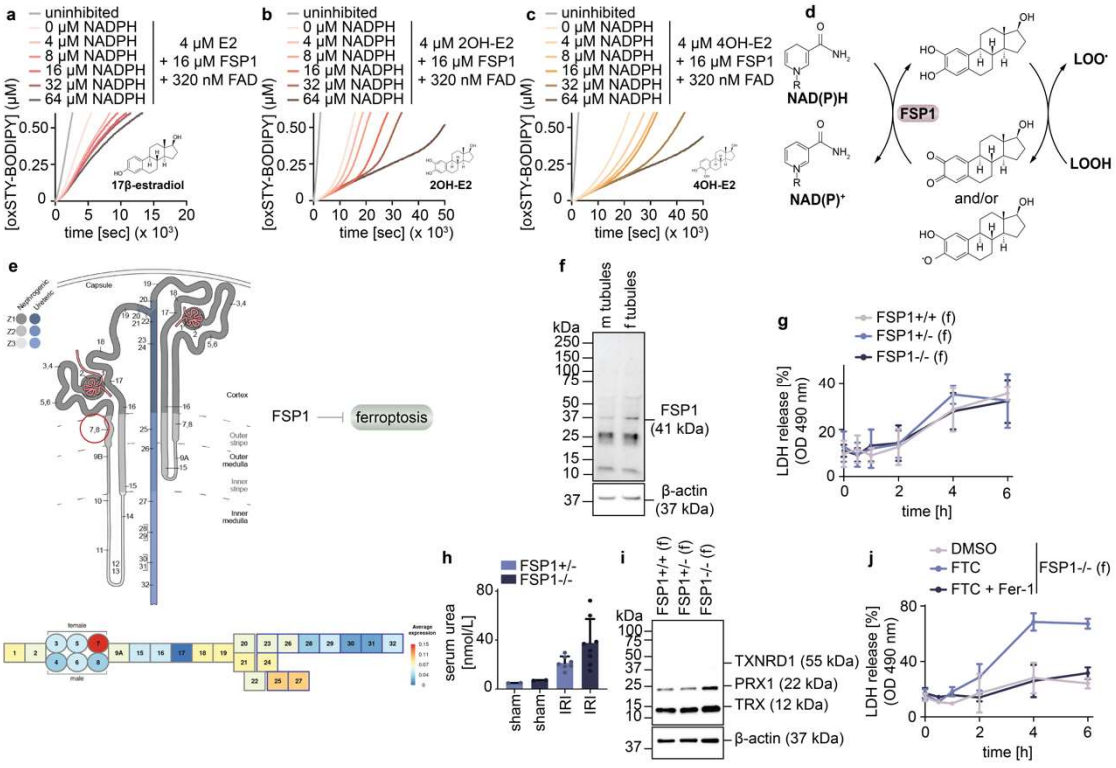

Figure 3. Sex-specific FSP1 expression in female tubules and FSP1-mediated regeneration of oxidized estradiol derivatives prevent female tubular necrosis. **a-c,** FENIX assay of 17β-estradiol, 2OH-E2 and 4OH-E2 in the presence of mFSP1 (16 nM), 4-64 µM NADPH and 320 nM FAD. **d,** Proposed mechanism of NAD(P)H dependent mFSP1-mediated regeneration of oxidised estradiol derivatives. **e**, Illustration of FSP1 expression along the nephron. The upper row with numbers 3, 5 and 7 represent the segments of proximal tubules from female mice, numbers 4, 6 and 8 represent the corresponding segments of male mice. **f,** Western blot analysis of FSP1 expression in lysates of freshly isolated tubules of male and female mice. **g,** LDH release over time of tubules of female mice of $FSP1^{+/+}$ (N = 4), $FSP1^{+/-}$ (N = 2) and $FSP1^{-/-}$ (N = 5) background. **h,** Serum levels of urea of $FSP1^{+/-}$ (N = 7) and $FSP1^{-/-}$ (N = 8) female mice treated with IRI. No significant differences were detected between the two groups. Data presented as mean ± SD. **i,** Western blot analysis of thioredoxin reductase 1 (TXNRD1), peroxiredoxin 1 (PRX1) and thioredoxin (TRX) in freshly isolated tubules from $FSP1^{+/+}$, $FSP1^{+/-}$ and $FSP1^{-/-}$ female mice. **j,** LDH release over time of $FSP1^{-/-}$ female tubules (N ≤ 3) treated with an inhibitor of the thioredoxin pathway, ferroptocide (FTC, 30 µM). 30 µM Fer-1 were used as the protection control.

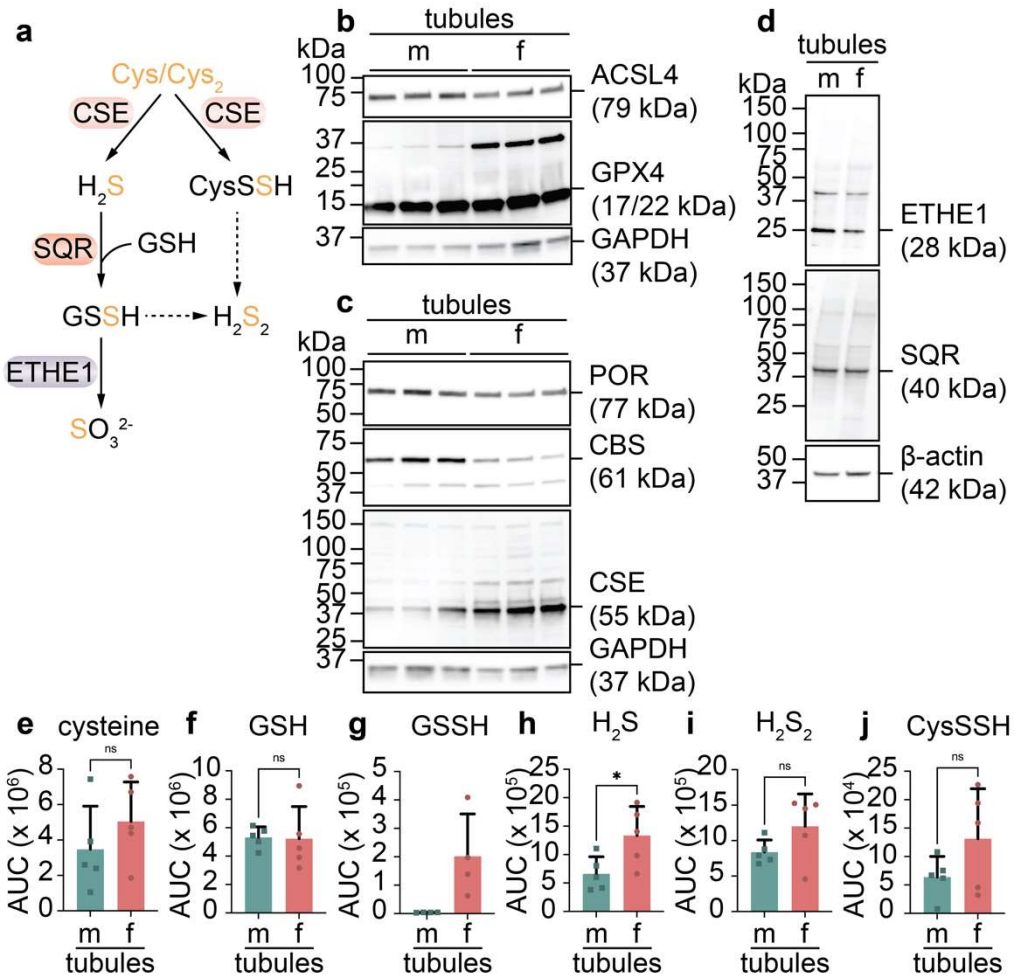

Figure 4. Sex specific renal tubular hydropersulfide metabolism in renal tubules. a, Simplified illustration of enzymatic hydropersulfide generation. **b,** Western blot analysis of ferroptosis-related enzymes, ACSL4 and GPX4, in lysates of freshly isolated tubules of wild type mice. GAPDH served as loading control. **c,** Western blot analysis of cytochrome P450 oxidoreductase (POR), cystathionine beta-synthase (CBS) and cystathionine gamma-lyase (CSE) in freshly isolated tubules of male and female wild type mice. GAPDH served as loading control. **d,** Western blot analysis of ETHE1 and SQR in freshly isolated tubules from male and female wild type mice. β-actin served as the loading control. **e-j,** Relative levels of sulfur metabolites related to hydropersulfide generation as assessed by LC/MS and presented as area under the curve (AUC) normalized to the protein content in each sample. Cys; cysteine, GSH; glutathione, GSSH; glutathione persulfide, H_2S; hydrogen sulfide, H_2S_2; hydrogen disulfide, CysSSH; cysteine persulfide. *P<0.05; ns = non-significant.

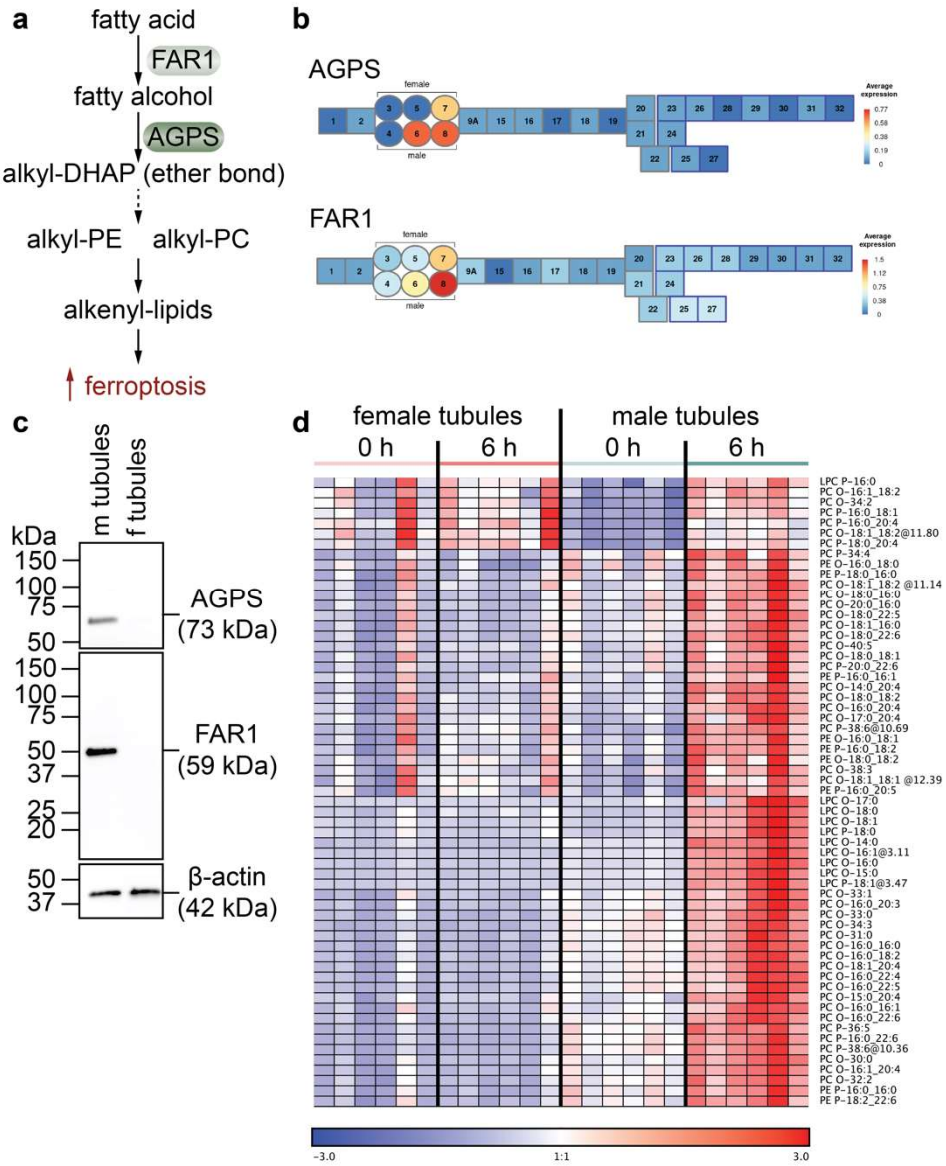

Figure 5. Exquisite ether lipid expression through the AGPS-FAR1-pathway in male mice. a, Illustration of the involvement of FAR1 and AGPS in the production of ether lipids that lead to a higher sensitisation to ferroptosis. **b,** RNA profiling of alkylglycerone phosphate synthase (AGPS) and fatty acyl-CoA reductase 1 (FAR1) expression in the different tubular compartments. **c,** Western blot analysis of AGPS and FAR1 in freshly isolated tubules from male and female mice. **d,** Heat map analysis of different classes of ether lipids obtained from freshly isolated tubules (0 h) and tubules that exhibited spontaneous necrosis (6 h) both from male and female mice.

Supplementary Information

Sex-specific Expression of Estradiol Derivatives, Hydropersulfides and Ether Lipids Regulates Ferroptosis Sensitivity of Kidney Tubules

Alexia Belavgeni[1], Wulf Tonnus[1], Francesca Maremonti[1], Sider Penkov[2], Melodie Mallais[3], Christine Gaillet[4], Anne Brucker[1], Danny Schilling[5,6], Lisa Schlicker[7], Nina Himmerkus[8], Shubhangi Gavali[1], Marlena Nastassja Schlecht[1], Karolin Flade[1], Jorunn Naila Becker[1], Mirela Tmava[1], Anne Haag[9], Christian Hugo[1], Almut Schulze[7], Bernd Plietker[9], Jan Ulrich Becker[10], Joel M. Weinberg[11], Svenja Lorenz[12], Bettina Proneth[12], Marcus Conrad[12], Raphaël Rodriguez[4], Stefan R. Bornstein[13-17], Tobias P. Dick[5,6], Derek A. Pratt[3], Maria Fedorova[2] and Andreas Linkermann[1, 18]

[1]Division of Nephrology, Department of Internal Medicine 3, University Hospital Carl Gustav Carus at the Technische Universität Dresden, Germany
[2]Center of Membrane Biochemistry and Lipid Research, University Hospital and Faculty of Medicine Carl Gustav Carus, Technische Universität Dresden
[3]Department of Chemistry and Biomolecular Sciences, University of Ottawa, Ottawa ON K1N 6N5, Canada
[4]Equipe Labellisée Ligue Contre le Cancer, Institut Curie, CNRS, INSERM, PSL Research University, Paris, France
[5]Division of Redox Regulation, German Cancer Research Center (DKFZ), DKFZ-ZMBH Alliance, Heidelberg, Germany
[6]Faculty of Biosciences, Heidelberg University, Heidelberg, Germany
[7]Division of Tumor Metabolism and Microenvironment, German Cancer Research Center (DKFZ), Heidelberg, Germany
[8]Institute of Physiology, Christian-Albrecht-University Kiel, Hermann-Rodewald-Str. 5, 24118 Kiel, Germany
[9]Chair of Organic Chemistry, Technische Universität Dresden, Dresden, Germany
[10]Institute of Pathology, University Hospital of Cologne, Cologne, Germany
[11]Division for Nephrology, University of Michigan Medical Center, Ann Arbor, MI, USA
[12]Institute of Metabolism and Cell Death, Helmholtz Zentrum München, Neuherberg, Germany
[13]Department of Internal Medicine 3, University Hospital Carl Gustav Carus at the Technische Universität Dresden, Dresden, Germany
[14]Diabetes and Nutritional Sciences, King's College London, London, UK.
[15]Center for Regenerative Therapies, Technische Universität Dresden, Dresden, Germany
[16]Paul Langerhans Institute Dresden of Helmholtz Centre Munich at University Clinic Carl Gustav Carus of TU Dresden Faculty of Medicine, Dresden, Germany
[17]Lee Kong Chian School of Medicine, Nanyang Technological University, Singapore, Singapore
[18]Division of Nephrology, Department of Medicine, Albert Einstein College of Medicine, Bronx, NY, USA

Supplementary Materials and Methods

Reagents

REAGENT or RESOURCE	SOURCE	IDENTIFIER
Antibodies		
ACSL4	Abcam	#ab155282
GPX4	Abcam	#ab125066
PRX (TXNRD1, PRX1, TRX)	Abcam	#ab184868
CBS	Thermofisher	#MA5-17273
CSE	Proteintech	#60234-1-Ig
POR	Abcam	#ab180597
FSP1	Provided by Marcus Conrad	n/a
AGPS	Invitrogen	# A115277
FAR1	Novus Biologicals	#A107209
ETHE1	GeneTex	GTX115707
SQR	Abcam	#ab71978
β-actin	Cell Signaling	#3700S
GAPDH	Cell Signaling	#2118S
Anti-mouse IgG; HRP-linked antibody	Cell Signaling	#7076S
Anti-rabbit IgG; HRP-linked antibody	Cell Signaling	#7074S
Compounds & chemicals		
Erastin (type I FIN)	Sigma Aldrich	#E7781
RSL3 (type II FIN)	Selleck Chemicals	#S8155
FIN56 (type III FIN)	Sigma Aldrich	#SML1740
FINO2 (type IV FIN)	Cayman Chemical	#25096
Ferrostatin-1 (Fer-1)	Merck Millipore	#341494
Ferroptocide	Provided by Paul J. Hergenrother	n/a
TNFα human	BioLegend	#570108
zVAD fmk	BD Biosciences	550377
Nec-1s (7-O-Cl-Nec-1)	Merck Millipore	#5.04297.0001
17β-estradiol	Sigma Aldrich	#E2758
Testosterone	Sigma Aldrich	#86500
2-hydroxyestradiol	Abcam	#ab142519
4-hydroxyestradiol	Cayman Chemicals	#31508
Annexin V, Alexa Fluor™ 647 conjugate	ThermoFisher Scientific	#A23204
7AAD	BD Biosciences	#559925
Annexin-V-FITC	BD Biosciences	#556420

Annexin-V binding buffer	BD Biosciences	#556454
Bradford assay	Thermo Fisher Scientific	#23225
ECL™ Prime Western Blotting System	Thermo Fisher Scientific	#GERPN2232
Kits		
LDH release assay	Promega	#G1780

Chemicals used for cell death assays were diluted in DMSO. 17β-estradiol, testosterone and 2-hydroxyestradiol were diluted in ethanol.

Cell lines and cell culture

EXPERIMENTAL MODELS	TYPE OF CELLS	SOURCE
CELL LINES		
HT1080 (human)	fibrosarcoma	ATCC (CCL-121)
NIH-3T3 (mouse)	embryonic fibroblasts	ATCC (CRL-1685)
CD10-135 (human)	kidney tubular epithelial cells	Provided by Rafael Kramann (5.2020)

Human HT1080 and mouse NIH-3T3 cell lines were purchased from the American Type Culture Collection, while CD10-135 were kindly provided by collaborators. All cell lines were grown in a humidified 5% CO_2 atmosphere at 37°C. HT1080 and NIH-3T3 cell lines were cultured in Dulbecco's modified Eagle medium (DMEM, Thermo Fisher) supplemented with 10% (v/v) FBS (Thermo Fisher, 41966029), 100 U/ml penicillin, and 100 µg/ml streptomycin (Pen/Strep, Thermo Fisher, 15140122). CD10-135 cells were cultured in Dulbecco's Modified Eagle Medium F-12 Nutrient Mixture with Glutamax (DMEM/F12 Glutamax, Thermo Fisher, 10565018) supplemented with 10% (v/v) FBS (Thermo Fisher, 41966029), 100 U/ml penicillin, and 100 µg/ml streptomycin (Pen/Strep, Thermo Fisher, 15140122).

Plating and treatment of cells

Detachment of HT1080, NIH-3T3 and CD10 cells was performed using Trypsin-EDTA (Gibco, 25200056). Cells were then washed twice and seeded in six-well plates (Sarstedt, 83.3920). All cells were seeded at 1 x 10^5 cells per well in six-well plates. Prior to the treatment, the medium was changed. Experiments were performed in a total volume of 1 ml.

Cell death assays

Ferroptosis was induced using established ferroptosis inducers (FINs): Type I FIN: erastin (Sigma Aldrich), type II FIN: RSL3 (Selleckchem), type III FIN: FIN56 (Sigma Aldrich) and type IV FIN: FINO2 (Cayman Chemical). Necrosis was additionally induced as previously described by the

thioredoxin reductase inhibitor ferroptocide[22]. Necroptosis in primary murine tubular cells was induced by treatement of 20 ng/ml TNFα (BioLegend) and 20 µM zVAD-fmk (BD Biosciences) (referred to as TZ treatment). Unless otherwise indicated, we used 5 µM erastin, 1.13 µM RSL3, 10 µM FIN56, 10 µM $FINO_2$ and 10 µM ferroptocide. After indicated time points, cells were collected and prepared for flow cytometry or Western blotting.

Flow cytometry

Cells were harvested and the pellets were washed twice in PBS and stained with 5 µl of 7AAD (BD Biosciences) and 5 µl of annexin-V-FITC (BD Biosciences) added to 100 µl annexin-V binding buffer solution (BD Biosciences). After 15 minutes, cells were recorded on the Fortessa LSRII with the FACS Diva 6.1.1 software (BD Biosciences) and subsequently analyzed with the FlowJo v10 software (Tree Star). The flow cytometry procedure was supported by the Flow Cytometry Core Facility of the CMCB Technology Platform at Technical University of Dresden (TU Dresden).

Western Blotting

Cells were lysed in ice-cold 50 mM Tris-HCl, pH 7.5, 150 mM NaCl, 1% NP-40, 5 mM EDTA supplemented with PhosSTOP™ (Merck), cOmplete™ (Merck), and 1 mM phenylmethylsulfonyl fluoride (PMSF) for 30 minutes on ice. Insoluble material was removed by centrifugation (14,000 g, 30 minutes, 4°C). Protein concentration was determined using a commercial BCA assay kit according to the instructions of the manufacturer (Thermo Fisher). Equal amounts of protein (typically 25 µg per lane) were resolved on a 4% – 15% gradient SDS/PAGE gel and transferred to a PVDF membrane (BIO-RAD). After blocking for 1 hour at room temperature, incubation with primary antibody was performed at 4°C overnight. Primary antibodies ACSL4 (Abcam, #ab155282), GPX4 (Abcam, #ab125066), CBS (Thermofisher, #MA5-17273), CSE (Proteintech, #60234-1-Ig), POR (Abcam, #ab180597), ETHE1 (GeneTex, #GTX115707), and SQR (Abcam, #ab71978) were diluted 1:1000 in 5% BSA (SERVA, #9048-46-8). Primary antibodies PRX (Abcam, #ab184868), AGPS (Invitrogen, #A115277), FAR1 (Novus Biological, #A107209), FSP1 (provided by Marcus Conrad) and β-actin (Cell Signaling, #3700S) were diluted 1:1000 in low fat milk (Roth, #68514-61-4). Secondary antibodies anti-mouse, HRP-linked antibody (Cell Signaling, #7076S), anti-rabbit, HRP-linked antibody (Cell Signaling, # 7074S) were applied at concentrations of 1:5000. Proteins were then visualized by enhanced chemiluminescence (ECL; Amersham Biosciences).

Isolation of primary murine renal tubules

Primary murine renal tubules were isolated following a modified previously published protocol[15]. In detail, murine kidneys were removed, washed with PBS, decapsualized and sliced in four to five slices. Kidney slices of each kidney were transferred in 2 ml reaction tube containing 2 mg/ml collagenase type II in incubation solution (48 µg/ml trypsin inhibitor, 25 µg/ml DNAse I, 140 mM NaCl, 0.4 mM

KH_2PO_4, 1.6 mM $K_2HPO_4 \cdot 3\ H_2O$, 1 mM $MgSO_4 \cdot 7\ H_2O$, 10 mM $CH_3COONa \cdot 3\ H_2O$, 1 mM a-ketoglutarate and 1.3 mM Ca-gluconate) and digested for 5 min at 37°C, 850 rpm. Due to the presence of damaged tubules, the first resulting supernatant was discarded and 1 ml of incubation solution was added to the kidney slices and digested for 5 min at 37°C, 850 rpm. The supernatant was collected and transferred in a 2 ml reaction tube containing 1 ml ice-cold sorting solution (0.5 mg/ml bovine albumin in incubation solution). The reaction tubes were left on ice for the tubules to precipitate. The supernatant was removed and the tubules were washed twice with ice-cold incubation solution. Once the tubules precipitated, the supernatant was removed and ice-cold sorting solution was added (the volume was adjusted depending on the number of samples needed for the experiment). Tubules were distributed in a twenty-four-well plate containing Dulbecco's Modified Eagle Medium F-12 Nutrient Mixture without glycine and phenol red (DMEM/F12, custom-made medium provided by Cell Culture Technologies LLC), supplemented with 0.01 mg/ml recombinant human insulin, 5.5 µg/ml human transferrin, 0.005 µg/ml sodium selenite (Na_2SeO_3) and 470 µg/ml linoleic acid (ITS+1, Sigma Aldrich, I2521), 50 nM hydrocortisone, 100 U/ml penicillin, and 100 µg/ml streptomycin (Pen/Strep, Thermo Fisher).

Spontaneous tubular necrosis and treatments of murine renal tubules

All experiments contain a negative control to assess LDH release at 0 h. No more than 10% LDH release in these negative controls was tolerated as quality control. Freshly isolated murine renal tubules were placed in twenty-four-well plates in Dulbecco's Modified Eagle Medium F-12 Nutrient Mixture without glycine and phenol red (DMEM/F12, custom-made medium provided by Cell Culture Technologies LLC), supplemented with 0.01 mg/ml recombinant human insulin, 5.5 µg/ml human transferrin, 0.005 µg/ml Na2SeO3 and 470 µg/ml linoleic acid (ITS+1, Sigma Aldrich, I2521), 50 nM hydrocortisone, 100 U/ml penicillin, and 100 µg/ml streptomycin (Pen/Strep, Thermo Fisher). After the indicated times, the medium of each well was collected and tubules were prepared for an LDH release assay (see LDH release assay section for further details).

In case of treatment of tubules, the medium or each well of a twenty-four-well plate was prepared with the compounds of interest. Tubules were added in each well and samples were prepared for the LDH release assay.

Outgrowth of primary murine renal tubules

Murine tubular cells were generated by outgrowth from freshly isolated renal tubules. Primary murine tubules were placed in six-well plates containing Dulbecco's Modified Eagle Medium F-12 Nutrient Mixture without glycine and phenol red (DMEM/F12, custom-made medium provided by Cell Culture Technologies LLC), supplemented with 0.01 mg/ml recombinant human insulin, 5.5 µg/ml human transferrin, 0.005 µg/ml Na2SeO3 and 470 µg/ml linoleic acid (ITS+1, Sigma Aldrich, I2521), 50 nM hydrocortisone, 100 U/ml penicillin and 100 µg/ml streptomycin (Pen/Strep, Thermo Fisher). After two days, the outgrown cells were washed with PBS and a fresh medium was added. When the number of

primary murine tubular cells reached 70% – 80% confluence, they were washed with PBS and treated with the different types of FINs or TZ (see the cell death assays section for information concerning concentrations). After 24 h, the medium was collected and each sample was prepared for an LDH release assay (see LDH release assay section for further details).

LDH release assay

The LDH release of cells or of freshly isolated kidney tubules was measured according to manufacturers' instructions at indicated time points. In brief, an aliquot of the supernatant was taken to assess the experimental LDH values. Subsequently, lysis solution was added for 45 min to induce maximal LDH release before another aliquot of the supernatant was taken. The supernatants were then incubated with CytoTox 96® Reagent for 15 min protected from light at room temperature before adding stop solution.

Absorbance was measured at 490 nm and calculated as $100 \times \frac{experimental\ LDH\ release}{max\ LDH\ release}$.

Time-lapse imaging

Videos of freshly isolated murine tubules stained with 50 nM SYTOX Green nucleic acid stain (Life Technologies) in the presence or absence of 150 nM BiotrackerTM 609 Red Ca^{2+} AM dye (Merck Millipore, #5.04297.0001) or 200 nM MitoTracker® Red FM (Invitrogen, #M22425) were obtained by using an oil-immersion 63x/0.3 EC Plan Neofluar objective. For these experiments, high-quality plastic-bottom slides (Ibidi 15 µ-slide 8-well, #80826) were used. The comparison of male and female murine tubules was performed using a 2.5×/0.3 EC Plan Neofluar objective, while the tubules were plated in a custom-made 3D chamber (see Generation of a 3D-printed double chamber section for further details). A 20x/0.3 EC Plan Neofluar objective was used for the observation of the outgrowth of primary tubular cells. An Axiovert 200M equipped with a large incubation chamber (37°C), 5% CO_2, and humidity control was used for all live imaging experiments. Transmitted light and fluorescent images (GFP BP filter cube, RFP double filter cube) were acquired using an Orca flash 4.0 camera. The live imaging procedure was supported by the Light Microscopy Facility, a Core Facility of the CMCB Technology Platform at Technical University of Dresden (TU Dresden).

Assessment of SYTOX positivity in freshly isolated renal tubules

Isolated renal tubules from male or female mice were incubated in a single 3D-printed well separated by a glass slide, stained with SYTOX green nucleic acid stain. Transmitted light and fluorescent time lapse images (GFP BP filter cube) were acquired (described in more detail in the time lapse imaging and processing of the time lapse data section above). Every 30 minutes, the images were assessed for the number of tubules exhibiting more than 90% of SYTOX green positivity. For the quantification of cell death propagation, tubules with less than 90% SYTOX positivity were not counted. Debris was not

included in the analysis. The total numbers of male and female tubules were visually counted. Data are presented as the percentage of tubules with equal or more than 90% of SYTOX positivity over time.

Electron microscopy

Murine tubules were isolated according to the above-mentioned protocol fixed in 4% buffered paraformaldehyde and afterwards fixed in glutaraldehyde and 1 hour of post-fixation/contrasting with osmium tetroxide. They were then embedded in Epon resin through graded ethanols and propylene oxide. Blocks were polymerized at 80°C overnight. Semi-thin sections were stained with methylene blue and azure blue. Thin sections were stained with lead citrate and uranyl acetate. Transmission electron microscopy was performed on a Zeiss Electron Microscope.

Generation of a 3D-printed double chamber

The 3D-printed chambers are composed of a border that includes a retainer designed to enclose the glass wall, effectively separating the two chambers[30]. The border of the chamber was printed on top of a silanized microscope slide and cured at 100°C for 30 minutes. The border was printed using a silicone elastomere (SE 1700; Dow Corning) using a 3DDiscovery bioprinter from RegenHU, employing a conical nozzle with an inner diameter of 250 μm. To achieve a printed line thickness of approximately 500 μm and a height of 8 mm, adjustments were made to the printing speed and extrusion pressure. Print layouts were developed using the BIOCAD software provided by RegenHU. To create a thinner line within the chambers, SE1700 was printed in the center at a higher printing speed, resulting in a thickness of approximately 200 μm, which is thinner than the border. The bonding of the glass wall to the retainer was achieved by manually applying SE1700 using a syringe with a conical needle. As for the glass wall itself, a cover slip measuring 20 x 20 mm with a thickness of 0.12 mm was cut down to a size of 8 x 20 mm. It was meticulously cleaned with ethanol and subjected to a 10-second treatment of air plasma using the Piezobrush PZ2-i, which is a cold-plasma generator equipped with a Nearfield nozzle from Relyon Plasma. The glass wall was then inserted into the retainer, pushed down until it made direct contact with the thin line of SE1700, and cured again at 100°C for 30 minutes. Afterwards, the structure was removed from the microscope slide, and both its bottom side and the inside of a six-well plate were treated with air plasma for approximately 10 seconds using the Piezobrush PZ2-i. The structure was attached to the six-well plate and kept at 60°C for 2 hours to facilitate bonding. In cases where certain areas of the border did not adhere well to the surface, those spots were sealed manually with SE1700. Subsequently, the structure was placed back at 60°C for an additional 4 hours. 3D-printed silicon double chambers were created by the Microstructure Facility, a Core Facility of the CMCB Technology Platform at TU Dresden.

Inhibited egg phosphatidylcholine liposome co-autoxidations (FENIX 1.0)

RTA only - Egg phosphatidylcholine liposomes (1.02 mM) (prepared as previously described[31]) STY-BODIPY (1.02 μM), and di-*tert*-undecyl hyponitrite (DTUN) (0.203 mM) in chelex-treated phosphate-buffered saline (cPBS) (12 mM phosphate, 150 mM NaCl, pH 7.4) were added to the wells of a Nunc black polypropylene round-bottomed 96-well microplate (295 μl). Using a 1 to 10 μL multichannel pipette, 5 μl of inhibitor solution in DMSO or vehicle only was then added to afford a final volume of 300 μl (final concentration of 1 mM egg-PC, 1 μM STY-BODIPY, 0.2 mM DTUN, and inhibitor varying between 2 and 16 μM). The reaction mixtures were manually mixed using a 100 to 300 μL multichannel pipette (set to 250 μl) and the microplate was inserted into a BioTek H1 Synergy microplate reader equilibrated to 37°C and vigorously shaken for 1 min followed by a 3.5-min delay. Fluorescence was then recorded (λ_{ex} = 488 nm; λ_{em} = 518 nm; gain = 60) every minute for 6 h. For *co-extruded samples*, egg phosphatidylcholine liposomes (final concentration 1.02 mM) [prepared as above] and inhibitor solution in DMSO (final concentration varied between 2.05–16.37 μM) were added to cPBS, vortexed, and re-extruded through a 100 nm polycarbonate membrane 15 times. This co-extruded mixture (782 μl) was subsequently diluted with STY-BODIPY (80 μM, 10 μl) and DTUN (20 mM, 8 μl) to yield a final volume of 800 μl (final concentration of 1 mM egg-PC, 1 μM STY-BODIPY, 0.2 mM DTUN, inhibitor varying between 2 and 16 μM in microplate well). The final solution was vortexed for 5 seconds and 300 μL was plated per well (2 wells plated per condition) and fluorescence was recorded on a BioTek H1 Synergy microplate as above.

RTA + reductant - Egg phosphatidylcholine liposomes (1.02 mM) (prepared as previously described[31]) STY-BODIPY (1.02 μM), inhibitor (4.07 μM) and di-*tert*-undecyl hyponitrite (DTUN) (0.203 mM) in chelex-treated phosphate-buffered saline (cPBS) (12 mM phosphate, 150 mM NaCl, pH 7.4) were added to the wells of a Nunc black polypropylene round-bottomed 96-well microplate (295 μl). Using a 1 to 10 μl multichannel pipette, 5 μl of reductant solution in cPBS or vehicle only was then added to afford a final volume of 300 μl (final concentration of 1 mM egg-PC, 1 μM STY-BODIPY, 4 μM inhibitor, 0.2 mM DTUN, and reductant concentration varies between 4 μM and 100 μM). The reaction mixtures were manually mixed using a 100 to 300 μl multichannel pipette (set to 250 μl) and the microplate was inserted into a BioTek H1 Synergy microplate reader equilibrated to 37°C and vigorously shaken for 1 min followed by a 3.5-min delay. Fluorescence was then recorded (λ_{ex} = 488 nm; λ_{em} = 518 nm; gain = 60) every minute for 15 h.

RTA + mFSP1 - Egg phosphatidylcholine liposomes (1.03 mM) (prepared as previously described[31]) STY-BODIPY (1.03 μM), inhibitor (4.14 μM), mFSP1 (16.55 nM) and FAD (331 nM) in pH 7.4 TBS buffer were added to the wells of a Nunc black polypropylene round-bottomed 96-well microplate (290 μl). Using a 1 to 10 μl multichannel pipette, 5 μL of NADPH solution in TBS or vehicle only was then added followed by 5 μl of DTUN solution (12 mM) in EtOH to afford a final volume of 300 μL (final concentration of 1 mM egg-PC, 1 μM STY-BODIPY, 4 μM inhibitor, 16 nM mFSP1, 320 nM FAD, 0.2 mM DTUN, and NADPH varying between 4 and 64 μM). The reaction mixtures were manually

mixed using a 100 to 300 µL multichannel pipette (set to 250 µl) and the microplate was inserted into a BioTek H1 Synergy microplate reader equilibrated to 37°C and vigorously shaken for 1 min followed by a 3.5-min delay. Fluorescence was then recorded (λ_{ex} = 488 nm; λ_{em} = 518 nm; gain = 60) every minute for 15 h. For *co-extruded samples,* egg-phosphatidylcholine liposomes (1.04 mM) and inhibitor in DMSO (4.15 µM) were added to TBS, vortexed and re-extruded through a 100 nm polycarbonate membrane 15 times. This co-extruded mixture (3594 µl) was then diluted with STY-BODIPY (1.74 mM, 2.14 µl), mFSP1 (48.9 µM, 1.22 µl) and FAD (0.5 mM, 2.38 µl) to achieve a final volume of 3600 µL of 'bulk-lipid' mixture. Then, 290 µL of 'bulk-lipid' mixture was plated in a Nunc black polypropylene round-bottomed 96-well microplate, followed by 5 µL of NADPH solution in TBS or vehicle. Finally, 5 µl of DTUN solution in EtOH (12 mM) was added (final concentrations in well: 1 mM egg-PC, 1 µM STY-BODIPY, 4 µM inhibitor, 16 nM mFSP1, 320 nM FAD, 4-64 µM NADPH, and 0.2 mM DTUN). The reaction mixtures were manually mixed and fluorescence was recorded on a BioTek H1 Synergy microplate as above.

Generation of 5,6,7,8-tetrahydronaphthalene-2,3-diol

To a pressure tube dried overnight at 150 °C in a drying oven is added under inert gas 2,3-dihydroxy-naphthalene (0.162 g, 1.01 mmol, 1.0 eq.), [Rh(cod)Cl]2 (75.0 mg, 0.015 mmol, 1.0 eq., 15 mol%) and Polymethylhydrosiloxane (0.18 ml, 3.00 mmol, 3.0 eq.) in methanol (3 ml). The reaction mixture is stirred at room temperature for two days. The solvent is removed in a vacuum and the crude product is purified over silica using the running mixture of iso-hexane/ethyl acetate (2.5:1) with an addition of 0.2 vol% triethylamine. The product is obtained as an off-white solid (118 mg, 72%). 40 mg of the product is purified via HPLC using the running mixture of iso-hexane/ethyl acetate (5:1) and obtained as a colorless solid (8.6mg, 21%). Rf(isoHex/EA: 3:1)=0.43 (Stained with anisaldehyde); ^{1}H NMR (CDCl3, 300 MHz): δ (ppm)= 6.57 (s, 2H), 4.80 (s, 2H), 2.66-2.61 (m, 4H), 1.76-1.72 (m, 4H)[32].

Measurement of sulfur-containing metabolites by ultra-performance liquid chromatography–mass spectroscopy

Briefly, the isolated tubules (see section 2.2.3. for isolation protocol) were washed twice with cold NaCl (0.9%) solution. Subsequently, any excess liquid was carefully removed. To ensure cell lysis, 200 µl of a 5 mM MBB (monobromobimane) solution in 50% MeOH was added to the tubules. The volume of MBB solution was adjusted based on the cell quantity, ensuring sufficient coverage to lyse all cells. The samples were then incubated in the dark at room temperature for 20 minutes. Following the incubation period, the tubules were snap frozen in liquid nitrogen, stored at -80 °C, and finally shipped to the designated location on dry ice for further analysis.

The cell suspension was spun down at 14,000 g for 10 minutes, and 3 µl of supernatant was applied to an Accucore 150 Amide HILIC HPLC column (100 × 2.1 mm, 2.6-µm particle size) equipped with a guard cartridge (at 30°C). Mobile phase 'A' was 5 mM ammonium acetate in 5% acetonitrile (CH_3CN);

mobile phase 'B' was 5 mM ammonium acetate in 95% CH_3CN. The liquid chromatography (LC) gradient program was: 98% B for 1 minute, followed by a linear decrease to 40% B within 5 minutes, then maintaining 40% B for 13 minutes, then returning to 98% B in 1 minute and finally 5 minutes at 98% B for column equilibration. The flow rate was 350 µl min^{-1}. The eluent was directed to the electrospray ionization (ESI) source of the Q Exactive (QE) MS from 0.5 minutes to 19 minutes after sample injection. Each sample was run with the parallel reaction monitoring (PRM) method for monobromobimane alkylated metabolites. PRM method: scan type: PRM positive mode; runtime: 0.5–10 minutes. $ddMS^2$ settings: resolution: 17,500; AGC target: 2×10^5; maximum injection time: 200 ms; loop count: 1; CE: 20, 50 and 80; isolation window: 1.2 *m/z*. For normalization among the samples, the protein pellets were dried on air and then dissolved in 200 µL 100 mM NaOH. The total protein content was determined by performing a BCA assay. PRM data were processed with Skyline[33] (21.2.0.425) and normalized to total protein.

NMR spectroscopy

To measure the interaction of 2OH-E2 and 4OH-E2 with Fe(II) or Fe(III), portions of 0.1 mol equivalent of a solution of $FeCl_2$ or $FeCl_3$ in MeOD (115mM) were added to a 5.8 mM solution of 2OH-E2 or 4OH-E2 in MeOD (1.0 mg of 2OH-E2 or 4OH-E2 in 600 µl MeOD) up to 1 mol equivalent into an NMR tube. ^1H NMR spectra were recorded on a 500 MHz Bruker spectrometer at 310 K in MeOD.

UPLC-MS

One drop from each corresponding NMR tube was added to a solution of H_2O:acetonitrile:formic acid 50:50:0.1 into a UPLC-MS vial. UPLC and low-resolution mass spectra (LRMS) were recorded on a Waters Acquity H-class equipped with a Photodiode Array Detector and SQ Detector 2 (UPLC-MS) fitted with a reverse phase column (Acquity UPLC BEH C18 1.7 µm, 2.1x50 mm) equipped with a van guard column. The gradient program was H_2O:acetonitrile:formic acid, linear gradient from 95:5:0.1 to 0:100:0.1 for 2.5 min, then maintain H_2O:acetonitrile:formic acid 0:100:0.1 for 1 min and finally return to H_2O:acetonitrile:formic acid 95:5:0.1 in 1 min. The flow rate was 0.6 ml min^{-1}.

Lipidomics analysis of murine renal tubules

Murine renal tubules were freshly isolated according to the isolation of primary murine renal tubules (see above, N = 6 for both sexes) and incubated in the presence of vehicle or 30 µM Fer-1 or 10 µM 2OH-E2. At 0h and 6 h the supernatant was carefully removed, and tubules were subsequently snap-frozen in liquid nitrogen before storage at -80 °C prior to lipid extraction. Lipids were extracted according to the Folch method as previously described in detail[34]. Briefly, SPLASH LIPIDOMIX (Avanti Polar Lipids Inc, 3 µL) and Cer/Sph Mixture I (Avanti Polar Lipids Inc, 3 µL) internal lipid standards were added to each sample, incubated on ice for 15 min followed by the addition of ice-cold methanol (300 µL) and ice-cold chloroform (600 µL). Samples were vortexed and incubated at 4 °C for 1h on a rotary shaker. Phase separation was induced by addition of ice-cold water (150 µL), followed

by vortexing, incubation at 4 °C (10 min), and centrifugation (1,000 x g, 10 min, 4 °C). All extraction solvents contained 1 µg/ml butylated hydroxytoluene (BHT) to avoid oxidation. The organic phase was collected and dried in a vacuum concentrator.

For LC-MS analysis, lipids were resuspended in 50 µL of isopropanol, centrifuged, and 40 µL were transferred to glass vials. Lipids were separated by reverse phase chromatography (Accucore C30 column; 150 mm x 2.1 mm 2.6 µM 150 Å, Thermo Fisher Scientific) using a Vanquish Horizon UHPLC system (Thermo Fisher Scientific) coupled on-line to a Orbitrap Exploris 240 mass spectrometer (Thermo Fisher Scientific) equipped with a HESI source. Lipids were separated at a flow rate of 0.3 ml/min (column temperature 50 °C) by the following gradient: 0-10 min, 30 % to 80 % B (curve 5); 10-27 min, 80 % to 95 % (curve 5); 27-31 min, 95 % to 100 % (curve 5); 31-37 min, isocratic 100 % (curve 5); 37-42 min, re-equilibration at 30 % B (curve 5). Eluent A consisted of acetonitrile:water (50:50, v/v, both ULC/MS-CC/SFC grade, Biosolve-Chemicals) and Eluent B of 2-propanol:acetonitrile:water (85:10:5, v/v/v), both containing 5 mM ammonium formate (MS grade, Sigma-Aldrich) and 0.1 % formic acid (ULC/MS-CC/SFC grade, Biosolve-Chemicals). Full MS settings were the following: spray voltage – 3500 V, sheath gas – 40 arb units, aux gas – 10 arb units, sweep gas – 1 arb unit, ion transfer tube – 300 °C, vaporizer temperature – 370 °C, EASY-IC run-start, default charge state – 1, resolution at m/z 200 – 120.000, scan range – m/z 200-1200, normalized AGC target – 100 %, maximum injection time – auto, RF lens – 35 %. Data-dependent acquisition (DDA) was based on a cycle time (1.3 s) at a resolution of 30.000, isolation window – 1.2 m/z, normalized stepped collision energies – 17,27,37 %, AGC target – 100 %, maximum injection time – 54 ms.

Lipid identification was performed using Lipostar2. Features with isotopic pattern and MS/MS spectrum were matched against the LIPID MAPS database and selected based on automatic approval (3-4 stars). After manual approval based on an established LC-MS/MS lipid identification strategy[35], lipid identities and chromatographic peak areas were exported and used for further analysis. Peak areas were normalized according to lipid standard abundances of the SPLASH LIPIDOMIX and Cer/Sph Mixture I and protein content of the samples. Normalized peak areas were auto-scaled using MetaboAnalyst 5.0. Lipids showing significant changes of abundance (ANOVA, $p<0,01$) were visualized through heat maps generated in Genesis 1.8.1 (Bioinformatics TU-Graz).

Mice

8–12-week-old male and female mice were co-housed 2 – 5 mice/cage in IVCs in our facility at the Medizinisch-Theoretisches Zentrum (MTZ) at the Medical Faculty of the Technical University of Dresden (TU Dresden). All wild-type mice (C57Bl/6N) were initially provided by Charles River, Sulzfeld, Germany, at the age of 6 – 7 weeks. $FSP1^{-/-}$ mice were described from our laboratory previously[15]. GSDMD-MLKL-dko mice were maintained in our facility after the first description[36]. $Gpx4^{fl/fl}$;ROSA26-CreERT2 were maintained in the Conrad laboratory in Munich as previously

described[16]. All experiments were performed according to German animal protection laws and were approved by ethics committees and local authorities in Dresden or Munich (Germany).

Induction of Gpx4 ko mice

For survival and endpoint studies, the tamoxifen-inducible conditional mouse strain Gpx4$^{fl/fl}$;ROSA26-CreERT2 was used, as previously described[16]. In brief, to induce *Gpx4* deletion, tamoxifen was first dissolved in Miglyol at a concentration of 20 mg/mL (Tamoxifen, Sigma T5648-1G; Miglyol, Caelo 3274-250 mL), whereupon 100 µl were injected i.p. on days 0 and 2. To detect potential gender-specific differences in survival time, animals were monitored daily and euthanized by cervical dislocation after presenting symptoms of acute kidney failure (humane endpoint), followed Kaplan-Meier survival analysis (GraphPad Prism 9 software). For the endpoint study, mice were again injected with tamoxifen twice, and serum and kidneys were collected at day 10. All animals were bred and maintained under standard SPF-IVC conditions with food and water ab libitum and all studies have been approved by the government of Upper Bavaria.

Bilateral kidney ischemia and reperfusion injury model (IRI)

Surgical protocol – All male and female mice were strictly matched for weight, age, and genetic background. Bilateral kidney ischemia and reperfusion injury (IRI) was performed as described in detail earlier[43]. In essence, 30 minutes prior to anesthesia, mice received a single dose of a ferrostatin (Fer-1 (10 mg/kg) or 2-OH estradiol (15 mg/kg)) or a corresponding vehicle control as indicated. 15 min prior to surgery, all mice received 0.1 µg/g body weight buprenorphine-HCl intraperitoneally for analgesia. Anesthesia was induced by the application of 3 l/min of volatile isoflurane with pure oxygen in the induction chamber of a COMPAC5 (VetEquip, the Netherlands) small animal anesthesia unit. After achieving a sufficient level of narcosis, typically within 2 min, mice were placed in a supine position on a temperature-controlled self-regulated heating system calibrated to 38°C and fixed with stripes at all extremities. Anesthesia was reduced to a maintenance dose of 1.5 l/min isoflurane. Breathing characteristics and levels of analgesia were closely assessed visually. The abdomen was opened layer-by-layer to create a 2 cm wide opening. Blunt retractors (Fine Science Tools (FST), Germany) were placed for convenient access. The caecum and gut were carefully mobilized and placed to the left side, where they were placed on a PBS-soaked sterile gauze. The second piece of PBS-soaked gauze was used to sandwich the gut, deliberately lifting the duodenum to visualize the aorta abdominalis. A cotton bud was used to gently push the liver cranially to fully access the right renal pedicle. With the use of a surgical microscope (Carl Zeiss, Jena, Germany), sharp forceps were used to pinch retroperitoneal holes directly cranially and caudally in the renal pedicle. Via this access, a 100 g pressure micro serrefine (FST 18055-03) was placed on the pedicle to induce ischemia and a timer was started. The cotton bud was removed, and the packed gut switched to the right side of the mouse to visualize the left renal pedicle. If required, the cotton bud was used to gently push aside the spleen or stomach. Once again,

retroperitoneal access was achieved by pinching holes with sharp forceps and another 100 g pressure micro serrefine was placed. The time between the placement of both serrefines was recorded (typically 40 s, controlled in all cases to under 1:00 min), the gut was returned into the abdominal cavity and the opening was covered with the two gauze pieces. Twenty-nine minutes after initially starting the timer, the retractors were put in place again and the gut again mobilized and packed to visualize the right kidney. After exactly 30 min (1 s tolerance), the vascular clamp was removed and the gut switched to the right side. After the recorded time difference, this clamp was removed as well. Reperfusion was determined visually for both sides before the gut was returned into the abdominal cavity. The parietal peritoneum and the cutis, respectively, were closed separately by continuous seams using a 6-0 monocryl thread (Ethicon). Isoflurane application was stopped immediately thereafter and 1 mL of pre-warmed PBS was administered intraperitoneally to compensate for any possible dehydration during surgery and to control for potential leakiness of the seams. The mice were divided into pairs of two and put back into the cages. 0.1 µg/g buprenorphine-HCl was administered every 8 h for analgesia. After a 48-h observation period, blood was collected by retroorbital puncture and the mice were sacrificed by neck dislocation. The right kidney was removed to be fixed for 24 h in 4% normal buffered formalin and transferred to 70% ethanol for storage at room temperature. The left kidney was removed and shock frozen in liquid nitrogen before transfer to −80°C for storage.

In this study, we applied two different doses of ischemia, a severe and a moderate model. The time of ischemia before the onset of reperfusion in the model of moderate IRI was 30 min (Fig. 2k–n, Fig. 3h Fig. S10k-m) and in the model of severe IRI was 38 min (Fig. 2k–n, Fig. 3h Fig. S10k-m), respectively. Otherwise, the two models are identical.

Histology

Organs were dissected as indicated in each experiment and put in 4% (vol/vol) neutral-buffered formaldehyde, fixated for 24 h, and then transferred to 70% ethanol for storage. In general, the kidneys were dehydrated in a graded ethanol series and xylene, and finally embedded in paraffin. Paraffin sections (3–5 µm) were stained with periodic acid–Schiff (PAS) reagent, according to standard routine protocol. Stained sections were analyzed using an Axio Imager microscope (Zeiss) at 100×, 200×, and 400× magnification. Micrographs were digitalized using an AxioCam MRm Rev. 3 FireWire camera and AxioVision ver. 4.5 software (Zeiss). Organ damage was quantified by two experienced pathologists in a double-blind manner on a scale ranging from 0 (unaffected tissue) to 10 (most severe organ damage). For the scoring system, tissues were stained with PAS, and the degree of morphological involvement in renal failure was determined using light microscopy. The following parameters were chosen as indicative of morphological damage to the kidney after ischemia-reperfusion injury (IRI): brush border loss, red blood cell extravasation, tubule dilatation, tubule degeneration, tubule necrosis, and tubular cast formation. These parameters were evaluated on a scale of 0–10, which ranged from not

present (0), mild (1–4), moderate (5 or 6), severe (7 or 8), to very severe (9 or 10). Each parameter was determined on at least five different animals.

Statistical analysis

Statistical analyses were performed with Prism 9 (GraphPad software, San Diego, CA, USA) using unpaired Student's t-test with Welch's correction. To test the null hypothesis of no difference between groups in the survival experiments we plotted the animals in a Kaplan-Meier curve and used the log-rank test for statistics. Mouse data on damage scores and serum levels of creatinine and urea were analyzed by a two-tailed parametric t-test. Data were considered significant when $*p \leq 0.05$, $**p \leq 0.01$, $***p \leq 0.001$ or $****p \leq 0.0001$.

Supplementary figures

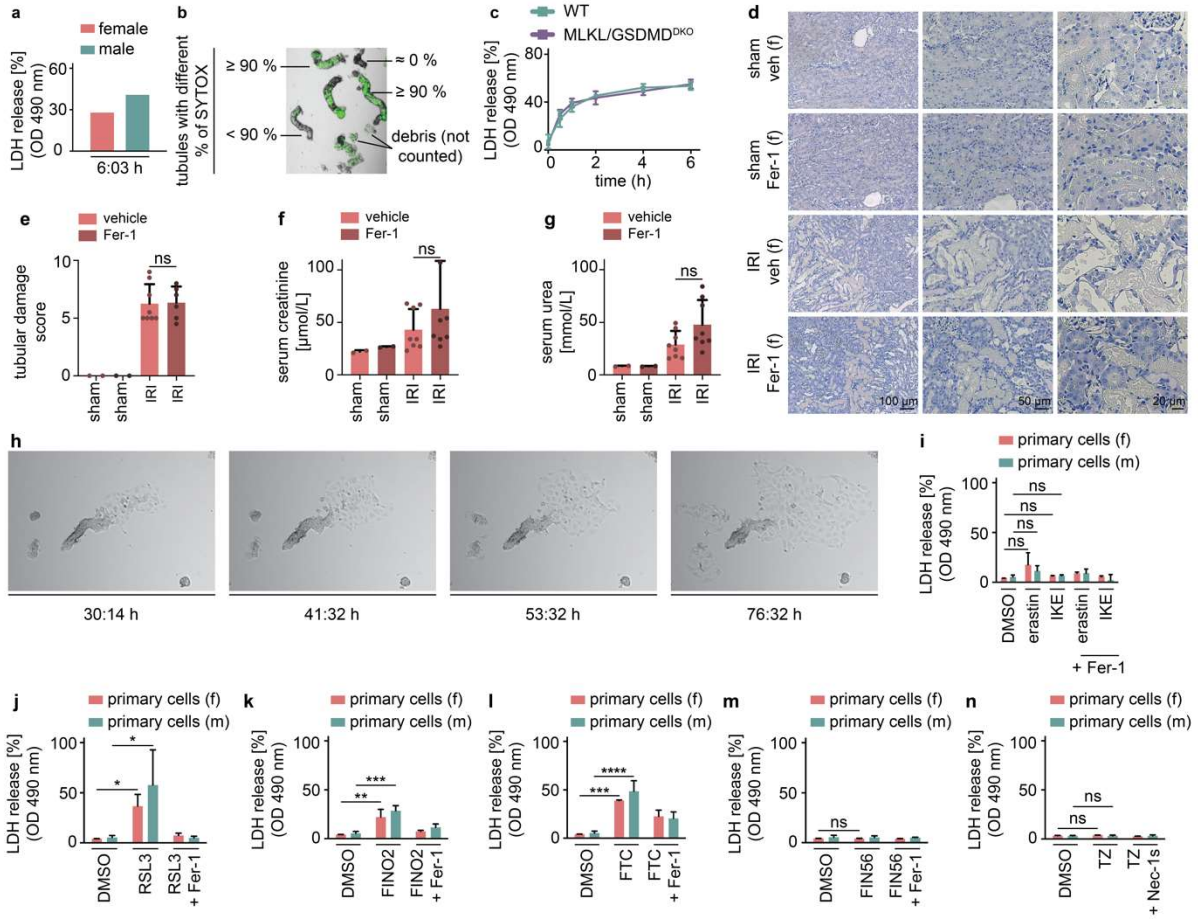

Figure S1 (to Fig 1). Tubules isolated from male mice and primary tubular cells from male and female mice are sensitive to ferroptosis. a, 6 h LDH release of the spontaneously dying tubules isolated from male and female mice used for the live imaging with the 3D chamber. **b**, Representative image of isolated tubules stained with SYTOX green indicating the tubules used for scoring the cell death propagation (CD). Only tubules showing 90% or more SYTOX green positivity were calculated for designated time points. **c,** LDH release of tubules isolated from WT (N = 4) and necroptosis/pyroptosis-deficient mice (MLKL/GSDMD^{DKO}) (N = 4) over time. **d,** Representative micrographs of PAS-stained histological sections of female wild type mice, injected with either vehicle or 10 mg/kg Fer-1 prior to IRI. **e,** Tubular damage score the aforementioned mice. **f,** Serum levels of creatinine and **g,** Urea levels of the aforementioned mice. **h**, Screenshots of isolated female tubules outgrowing primary tubular cells over time. **i-l**, LDH release of primary tubular cells outgrown from female or male tubules treated with erastin (5 µM) or IKE (5 µM), **j,** RSL3 (1.13 µM), **k,** FINO2 (10 µM), **l,** ferroptocide (FTC, 10 µM), **m,** FIN56 (10 µM) for 24 h. Fer-1 (1 µM) was used as a protection control for ferroptosis. Each experiment was performed three times. **n.** LDH release of primary tubular cells outgrown from female or male tubules treated with TNF-α (20 ng/ml) and zVAD-fmk (20 µM) for 24 h. Nec-1s (10 µM) was used as a protection control for necroptosis. Data presented as mean ± SD. *$p < 0.05$; **$p < 0.01$; ns = non-significant.

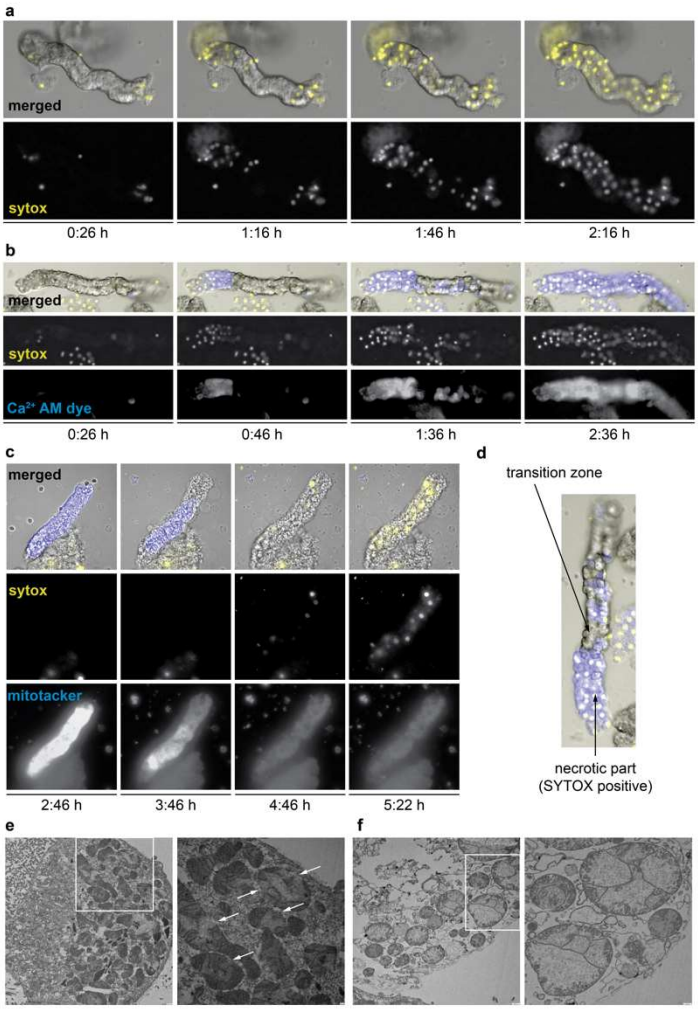

Figure S2 (to Fig 1). Cell death propagation in male isolated renal tubules. a, Screenshots of isolated tubule of male mouse stained with SYTOX green (pseudo-coloured in yellow). Single green channel images in grayscale are added to show the propagation of cell death. **b,** Isolated tubule from male mouse stained with SYTOX green (pseudo-coloured in yellow) and Ca^{2+} AM dye (pseudo-coloured in blue). Single green and red channel images in grayscale are added to show the parallel propagation of cell death for both dyes. **c,** Isolated tubule from male mouse stained with SYTOX green (pseudo-coloured in yellow) and mitotracker (pseudo-coloured in blue). **d,** Representation of the two necrotic zones of a tubule dying by spontaneous necrosis. The non-stained part for SYTOX green is the transition zone, while the SYTOX green-stained part of the tubule is the necrotic part. **e,** Electron microscopy images of the transition zone of the tubule. **f,** Electron microscopy image of the necrotic part of the tubule. The higher resolution focuses on ballooned mitochondria with the cristae flanking the mitochondrial membrane.

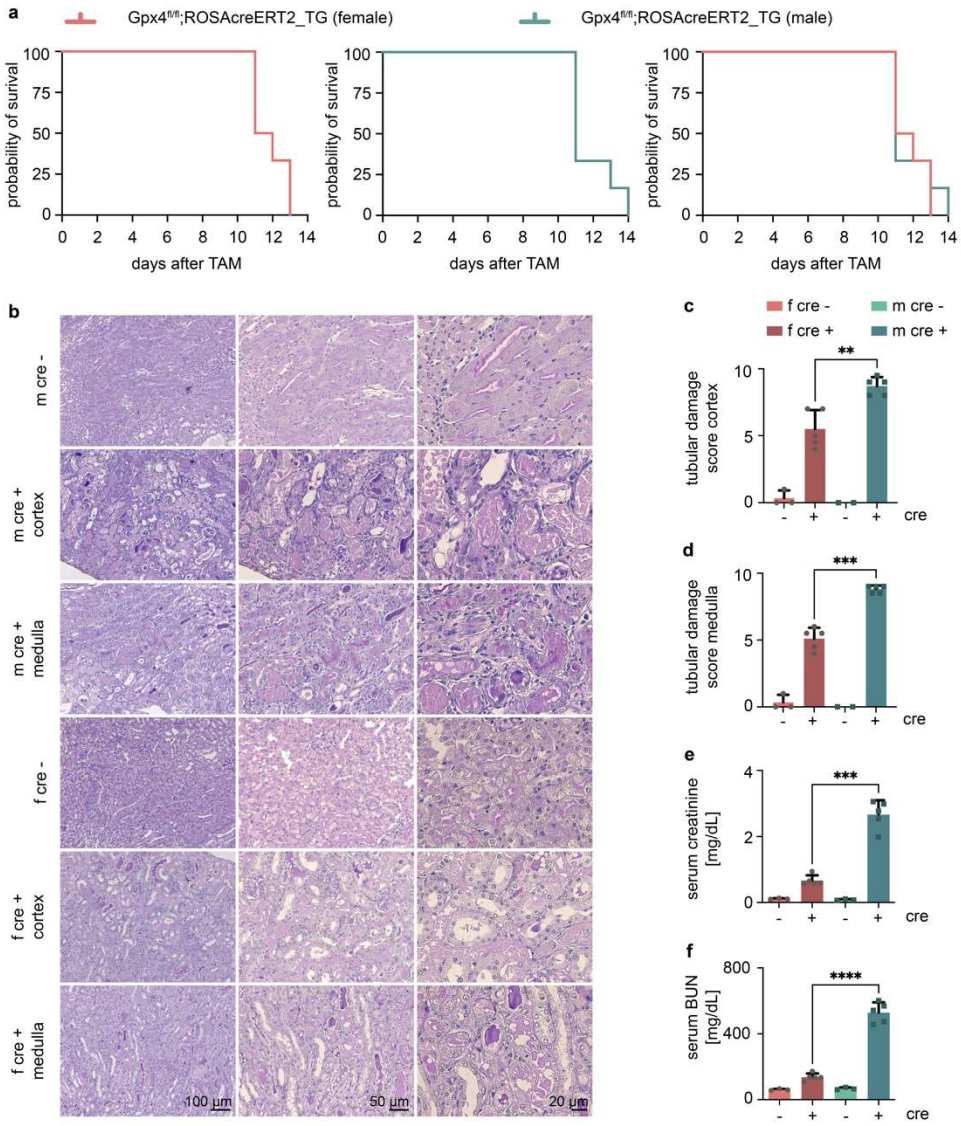

Figure S3 (to Fig 1). Sex specific kidney injury following tubular GPX4-deletion. a, Survival of Gpx4-inducible knock-out male and female mice (N = 6). **b,** Representative micrographs of PAS-stained sections of male or female cre- or cre+ (induced Gpx4 KO for 10 days). For cre+ mice representative images from the cortex and the medulla are shown, revealing the higher tubular damage in both compartments of the kidney in male mice. **c,** Tubular damage score in the cortex and **d,** the medulla of the aforementioned mice. **e,** Serum levels of creatinine and **f,** BUN assessment of the aforementioned mice. TAM; Tamoxifen. Data presented as mean ± SD. *$p < 0.05$; **$p < 0.01$; ***$p < 0.001$; ****$p < 0.0001$.

Figure S4 (to Fig 2). 17β-estradiol protects three different cell lines from ferroptosis inhibition and from inhibition of the thioredoxin pathway. a, Flow cytometry analysis of HT1080 cells treated simultaneously with 17β-estradiol (10 μM) and erastin (5 μM), **b,** FIN56 (10 μM), **c,** FINO2 (10 μM) or **d,** ferroptocide (FTC, 10 μM). **e,** Flow cytometry analysis of NIH-3T3 cells treated simultaneously with 17β-estradiol (10 μM) and erastin (5 μM), **f,** FIN56 (10 μM), **g,** FINO2 (10 μM) or **h,** ferroptocide (FTC, 10 μM). **i,** Flow cytometry analysis of CD10 cells treated simultaneously with 17β-estradiol (10 μM) and erastin (5 μM), **j,** RSL3 (1.13 μM), **k,** FIN56 (10 μM), **k,** FINO2 (10 μM) or **m,** ferroptocide (FTC, 10 μM). In all cases, cells were stained with annexin V and 7AAD.

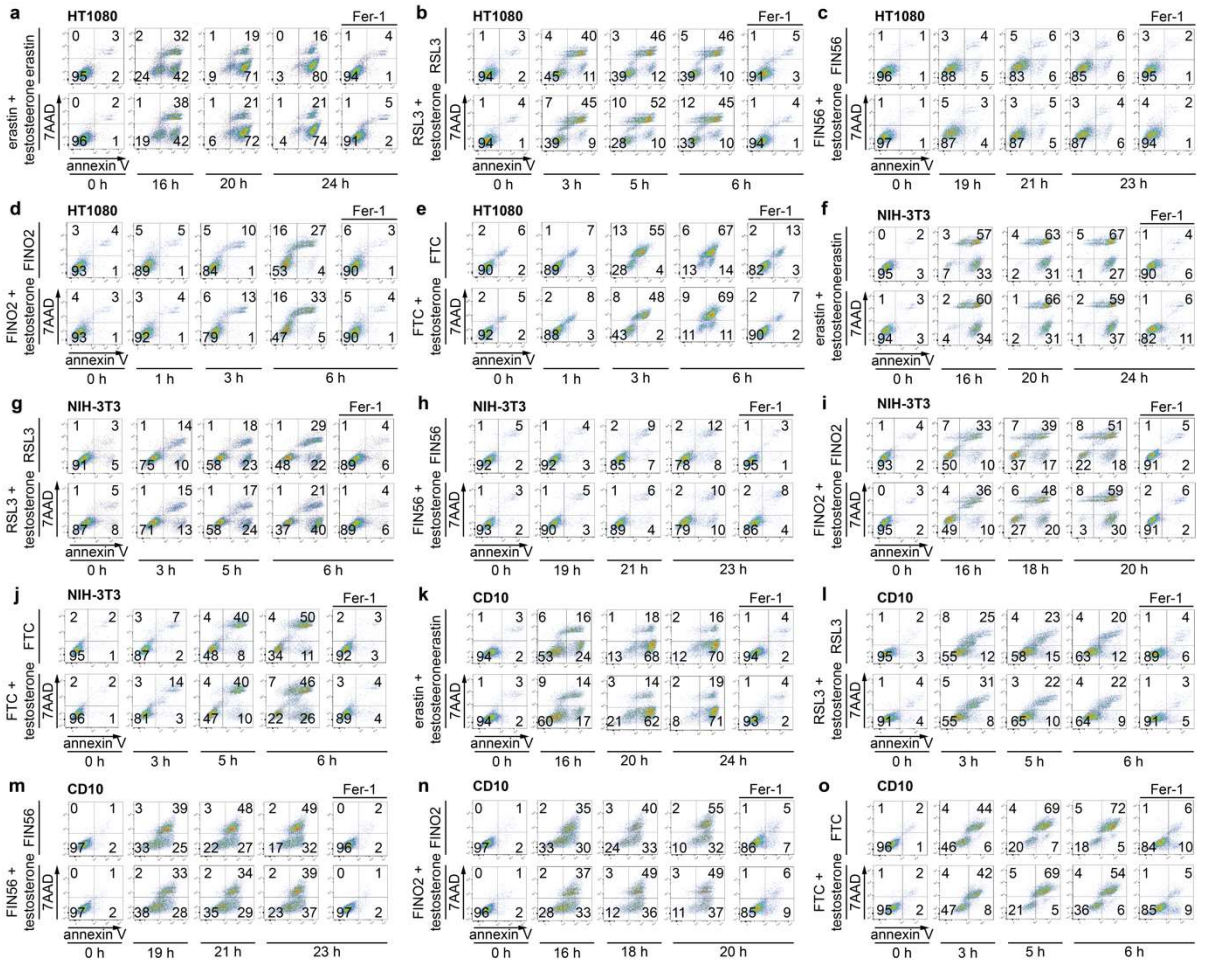

Figure S5 (to Fig 2). Testosterone does not affect ferroptosis or necrosis-treated ferroptosis-sensitive cells. a, Flow cytometry analysis of HT1080 cells treated simultaneously with testosterone (10 μM) and erastin (5 μM), **b,** RSL3 (1.13 μM), **c,** FIN56 (10 μM), **d,** FINO2 (10 μM) or **e,** ferroptocide (FTC, 10 μM). **f,** Flow cytometry analysis of NIH-3T3 cells treated simultaneously with testosterone (10 μM) and erastin (5 μM), **g,** RSL3 (1.13 μM), **h,** FIN56 (10 μM), **i,** FINO2 (10 μM) or **j,** ferroptocide (FTC, 10 μM). In all cases, cells were stained with annexin V and 7AAD. **k,** Flow cytometry analysis of CD10 cells treated simultaneously with testosterone (10 μM) and erastin (5 μM), **l,** RSL3 (1.13 μM), **m,** FIN56 (10 μM), **n,** FINO2 (10 μM) or **o,** ferroptocide (FTC, 10 μM). In all cases, cells were stained with annexin V and 7AAD.

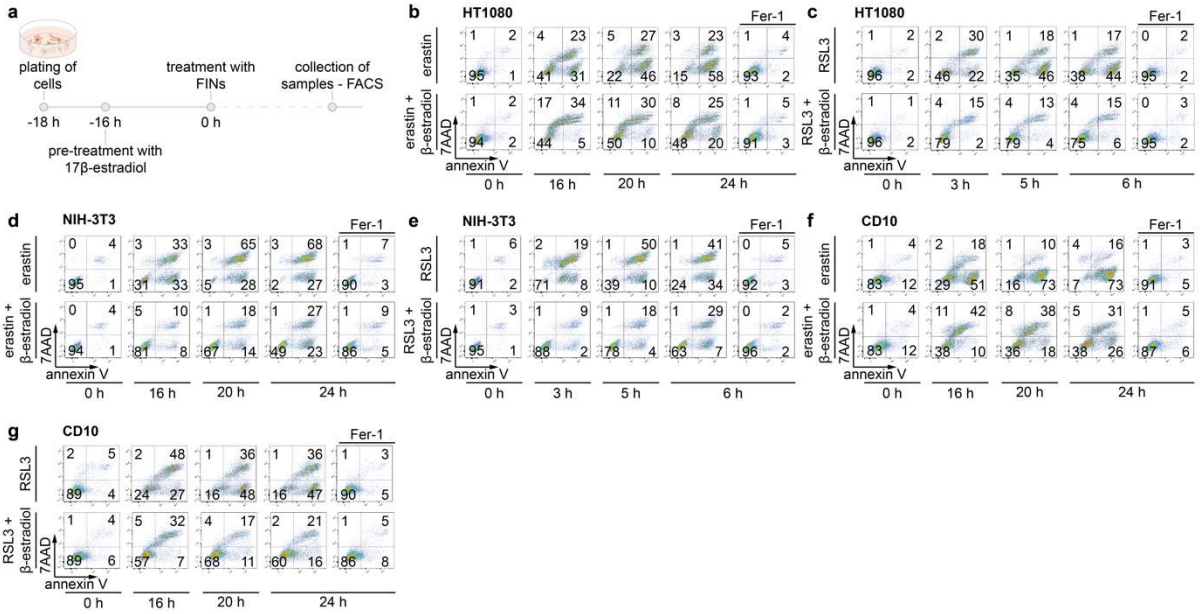

Figure S6 (to Fig 2). Pre-treatment of different cell lines with 17β-estradiol rescues from type I and type II ferroptosis induction. a, Schematic presentation of the protocol followed for the pre-treatment of cells with 17β-estradiol. **b,** Flow cytometry analysis of HT1080 cells pre-treated with 17β-estradiol (10 μM) for 16 h and then treated with erastin (5 μM) or **c,** RSL3 (1.13 μM). **d,** Flow cytometry analysis of NIH-3T3 cells pre-treated with 17β-estradiol (10 μM) for 16 h and then treated with erastin (5 μM) or **e,** RSL3 (1.13 μM). **f,** Flow cytometry analysis of CD10 cells pre-treated with 17β-estradiol (10 μM) for 16 h and then treated with erastin (5 μM) or **g,** RSL3 (1.13 μM). In all cases, cells were stained with annexin V and 7AAD.

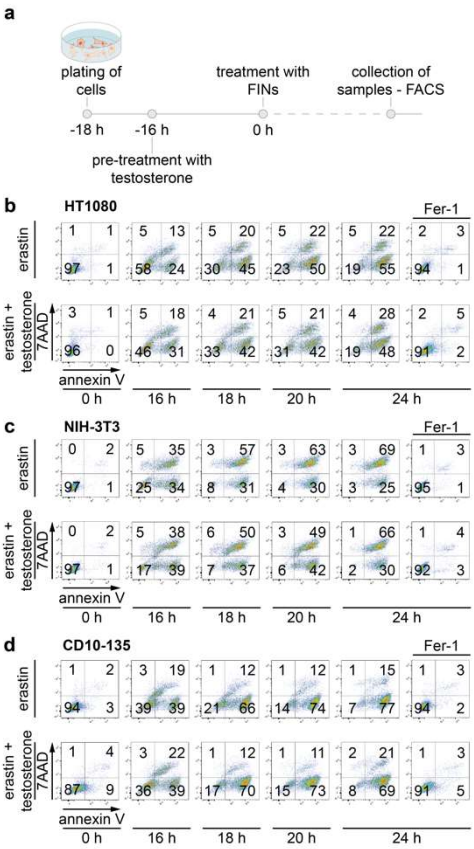

Figure S7 (to Fig 2): Pre-treatment of different cell lines with testosterone does not affect type-I-induced ferroptosis. a, Schematic presentation of the protocol followed for the pre-treatment of cells with testosterone. **b,** Flow cytometry analysis of HT1080, **c,** NIH-3T3 and **d,** CD10 pre-treated with testosterone (10 μM) for 16 h and then treated with erastin (5 μM) for different time points. In all cases, cells were stained with annexin V and 7AAD.

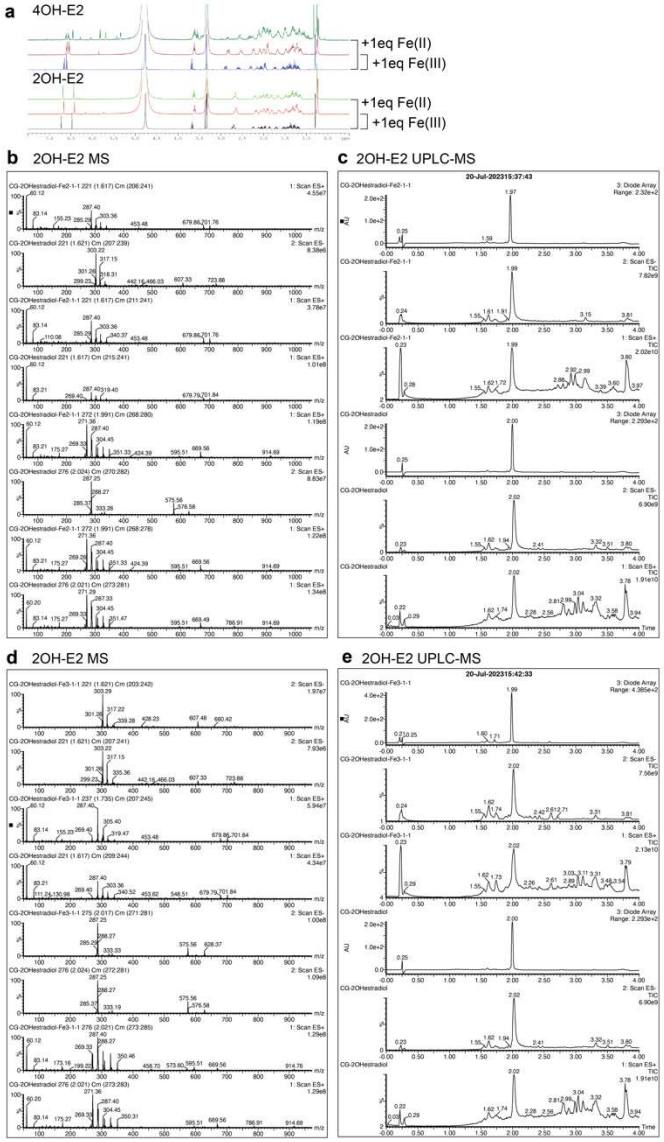

Figure S8 (to Fig 3). 2OH-E2 does not bind to Fe(II). a, NMR analysis investigating the capacity of 4OH-E2 and 2OH-E2 to bind to either Fe(II) or Fe(III). No interaction is shown between 2OH-E2 and Fe(II) or Fe(III), however 4OH-E2 shows a non-negligeable interaction with Fe(II), but not Fe(III).**b,** Mass spec analysis and **c,** UPLC-MS of 2OH-E2 capacity to bind to Fe(II). **d,** Mass spec analysis and **e,** UPLC-MS of 2OH-E2 capacity to bind to Fe(III).

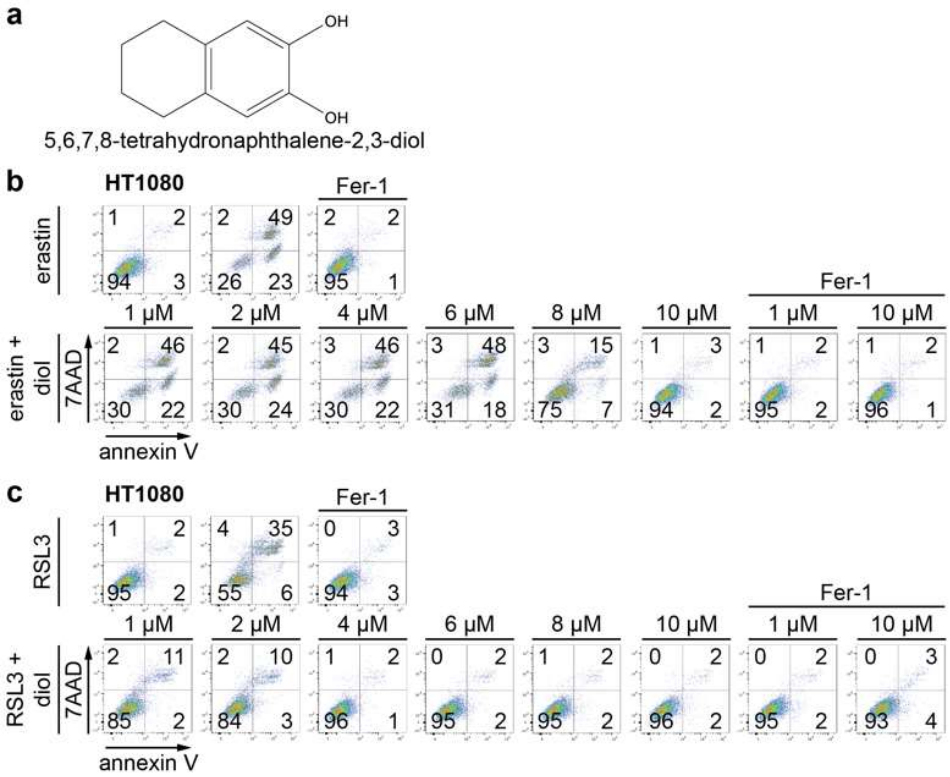

Figure S9 (to Fig 2). 5,6,7,8-tetrahydronaphthalene-2,3-diol protects HT1080 from type I and II ferroptosis inducers. a, Chemical structure of 5,6,7,8-tetrahydronaphthalene-2,3-diol **b,** Flow cytometry analysis of HT10080 cells treated with different concentrations of diol (abbreviation of 5,6,7,8-tetrahydronaphthalene-2,3-diol) and co-treated with erastin (5 μM). **c,** Flow cytometry analysis of HT10080 cells treated with different concentrations of diol and co-treated with RSL3 (1.13 μM). In all cases, cells were stained with annexin V and 7AAD.

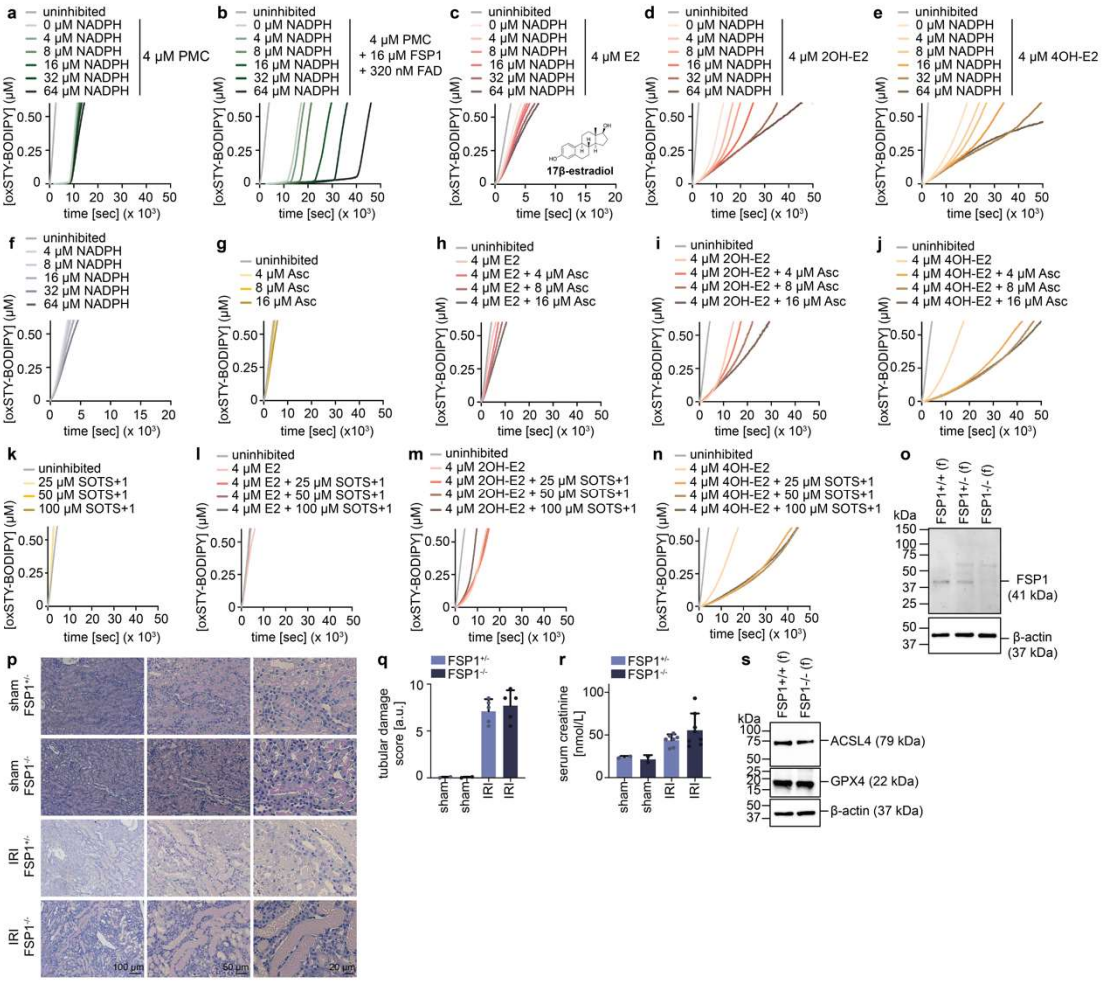

Figure S10 (to Fig 3). Experimental regeneration of estradiol derivatives by ascorbate. a, FENIX assay of PMC in the presence of 4-64 µM NADPH. **b,** FENIX assay of PMC in the presence of mFSP1 (16 nM), 4-64 µM NADPH and 320 nM FAD. **c-e,** FENIX assay of 17β-estradiol, 2OH-E2 and 4OH-E2 in the presence of 4-64 µM NADPH. **f,** FENIX assay of 4-64 µM NADPH, serving as control of panels a-e. **g,** FENIX assay of ascorbate (Asc) serving as control showing no regenerative capacity in the absence of a compound that can be oxidised. **h-j,** FENIX assay of ascorbate in the presence of 17β-estradiol (E2), 2OH-E2 and 4OH-E2. **k,** FENIX assay of superoxide thermal source (SOTS-1) serving as control showing no regenerative capacity in the absence of a compound that can be oxidised. SOTS-1 thermally decomposes to yield two equivalents of superoxide, which is in equilibrium with its conjugate acid hydroperoxyl radical (HOO•). **l-n,** FENIX assay of SOTS-1 in the presence of 17β-estradiol (E2), 2OH-E2 and 4OH-E2. **o,** Western blot analysis of the FSP1 expression in freshly isolated tubules from $FSP1^{+/+}$, $FSP1^{+/-}$ and $FSP1^{-/-}$ female mice. β-actin served as loading control. **p,** Representative microphotographs of periodic acid-Schiff (PAS)-stained histological sections of sham or IRI-treated $FSP1^{+/+}$ and $FSP1^{-/-}$ female mice. **q,** Tubular damage score of the mice mentioned in l. **r,** Serum levels of creatinine of sham (N = 2) or IRI-treated $FSP1^{+/+}$ (N = 7) and $FSP1^{-/-}$ (N = 8) female mice mentioned in l. **s,** Western blot analysis of the ACSL4 and GPX4 expression in tubules isolated from $FSP1^{+/-}$ and $FSP1^{-/-}$ female mice. β-actin served as loading control.

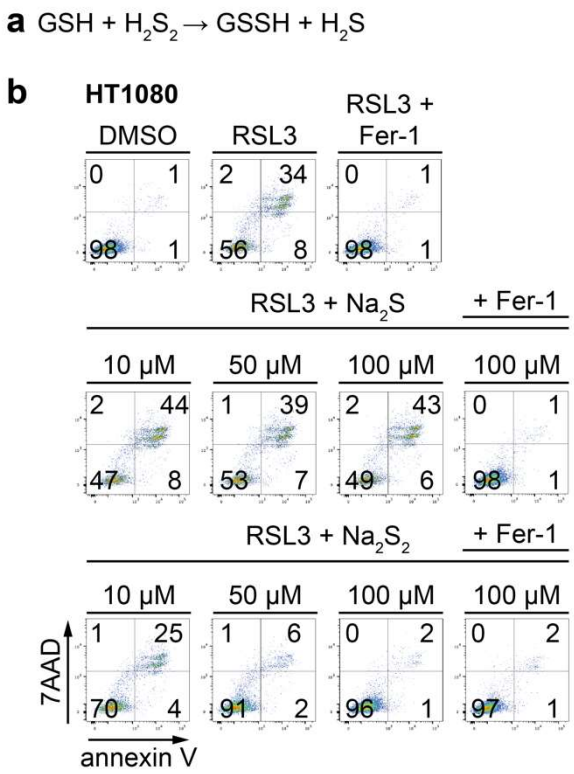

Figure S11 (to Fig 4). Effects of Na_2S and Na_2S_2 on RSL3-induced ferroptosis a, Mechanism by which the persulfide donor H_2S_2 converts GSH into GSSH. **b,** HT1080 cells treated with 1.13 µM RSL3 and co-treated with different concentrations of Na_2S or Na_2S_2. Notice that only Na_2S_2 shows protective effects, since it is a direct hydropersulfide donor in contrast to Na_2S. Fer-1 was used as the protection control. In all cases, cells were stained with annexin V and 7AAD.

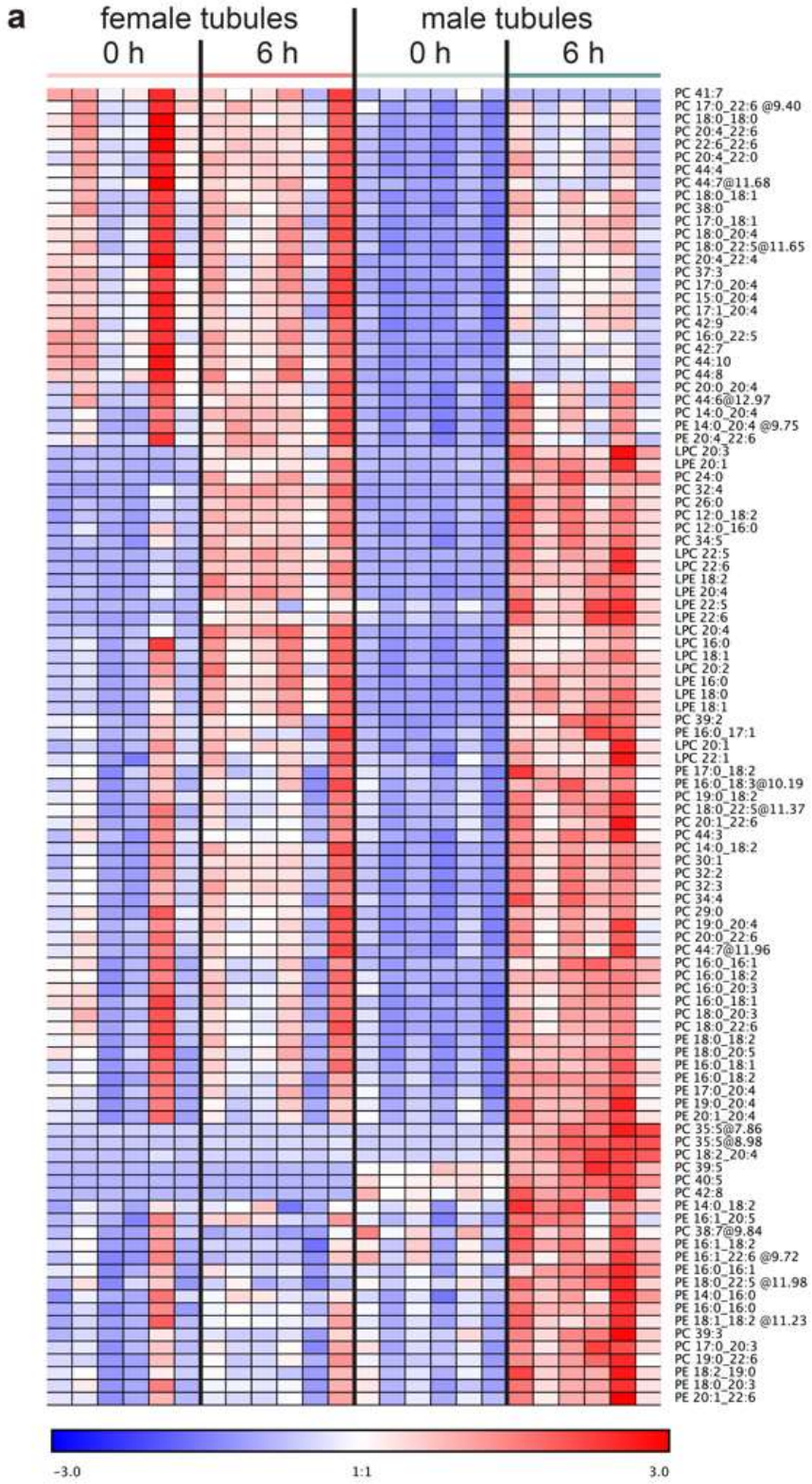

Figure S12 (to Fig 5). Ester lipidomics analysis of freshy isolated male and female kidney tubules. a, Heat map analysis of different classes of ester lipids obtained from freshly isolated tubules (0 h) and tubules that exhibited spontaneous necrosis (6 h) both from male and female mice.

Figure S13: Graphical abstract / summary slide

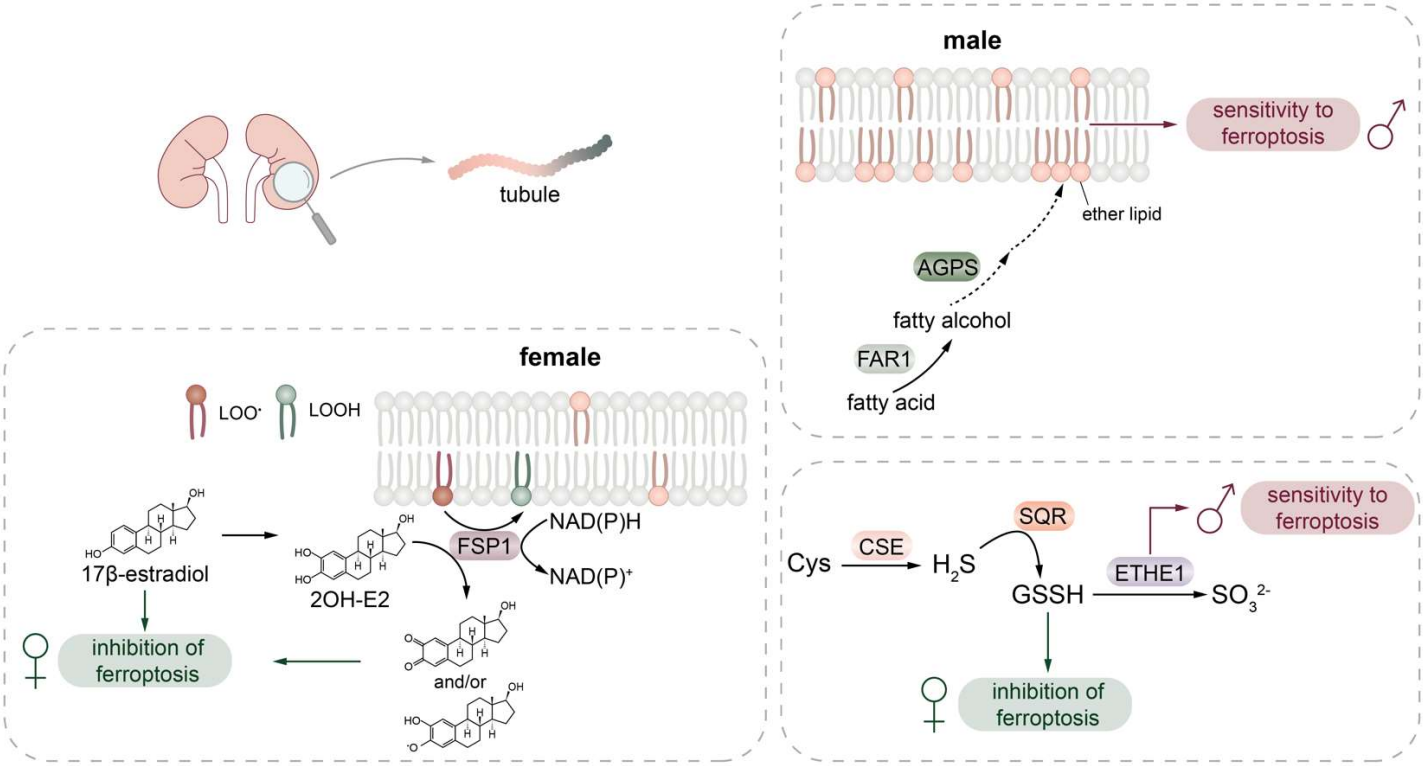

Supplementary videos

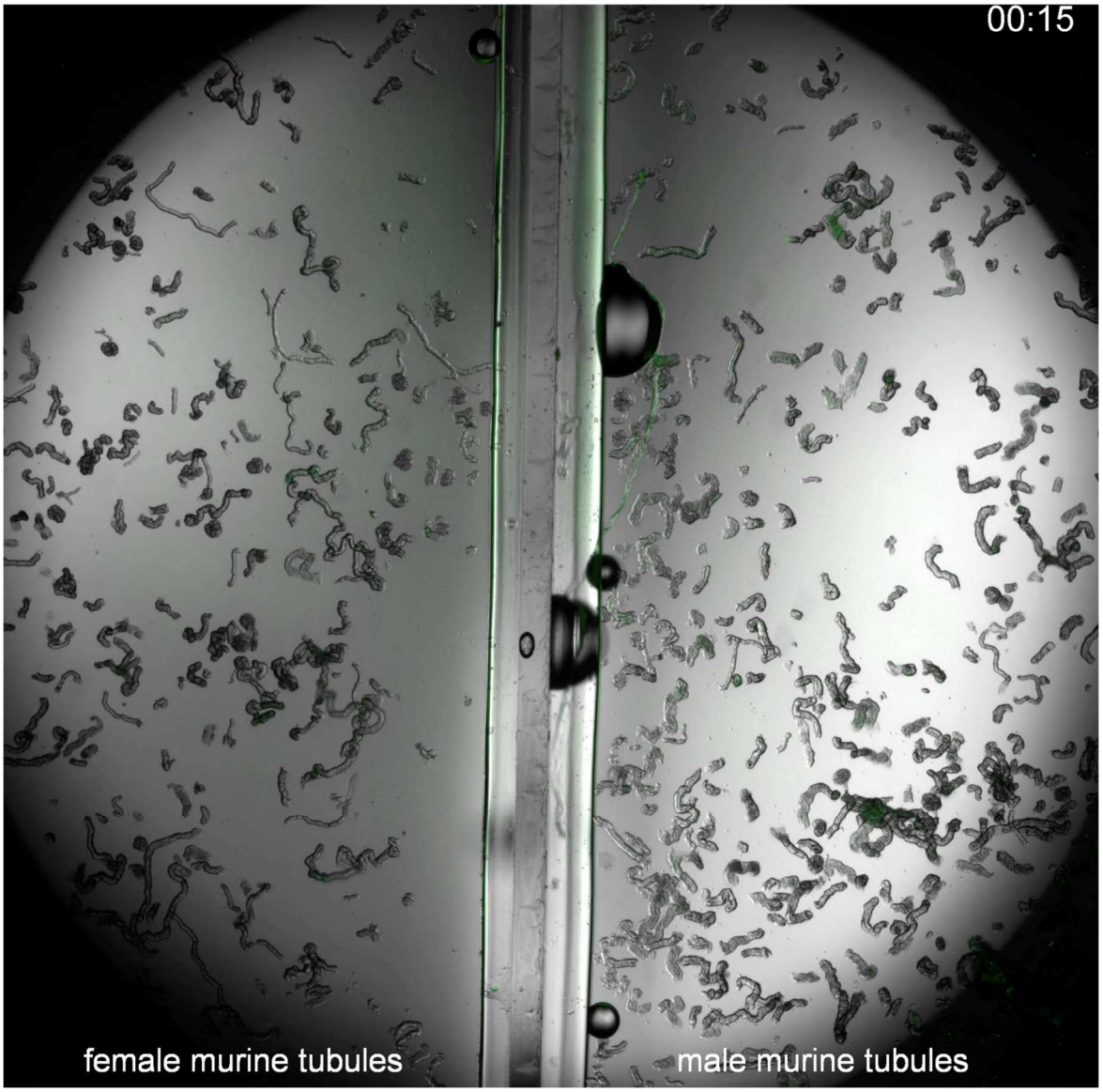

Video S1. Freshly isolated tubules from female (left side) and male (right side) mice exhibiting spontaneous necrosis. SYTOX green staining was used as a necrotic cell marker.

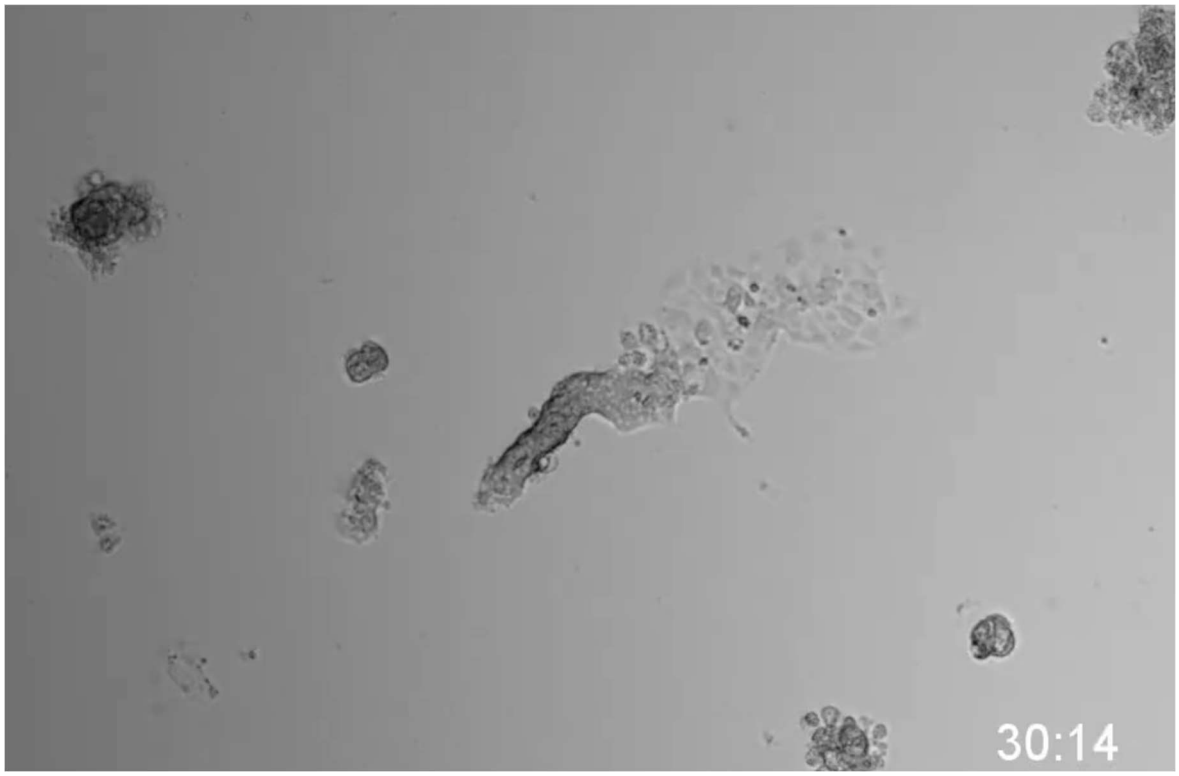

Video S2. Outgrowth of primary tubular cells from female tubules.

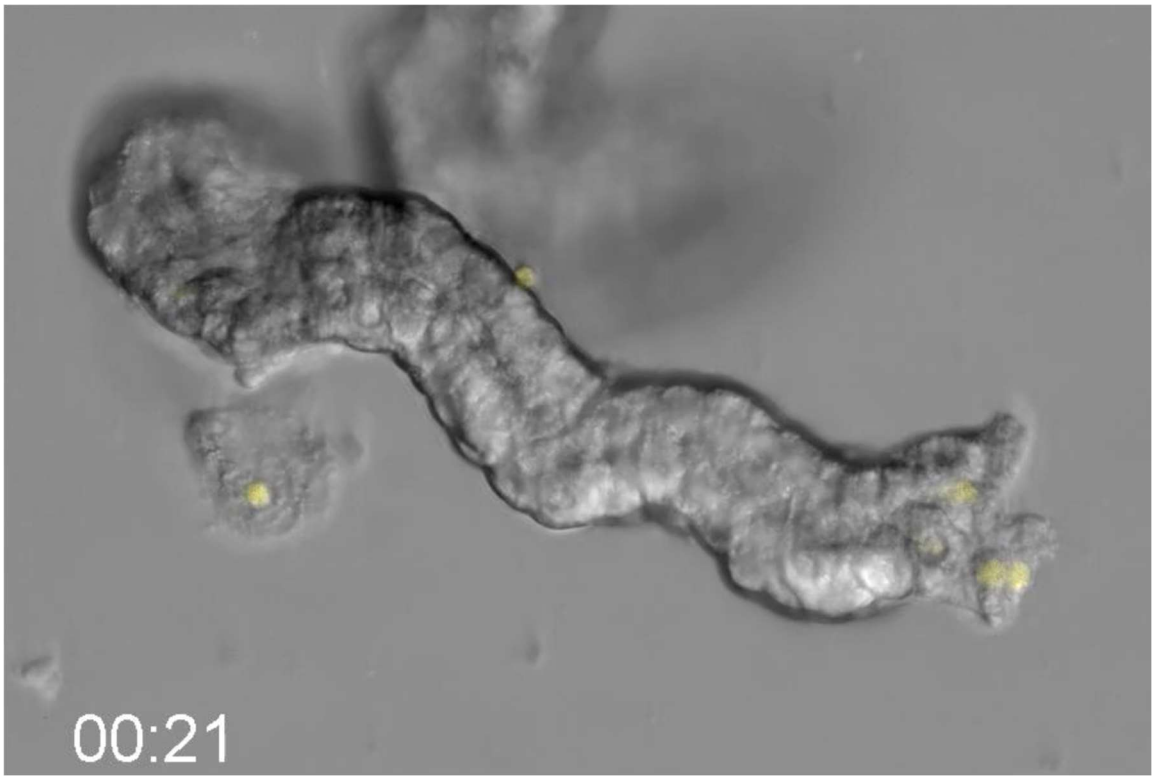

Video S3. Spontaneous necrosis of freshly isolated tubules from male mouse stained with SYTOX green (pseudo-colored in yellow).

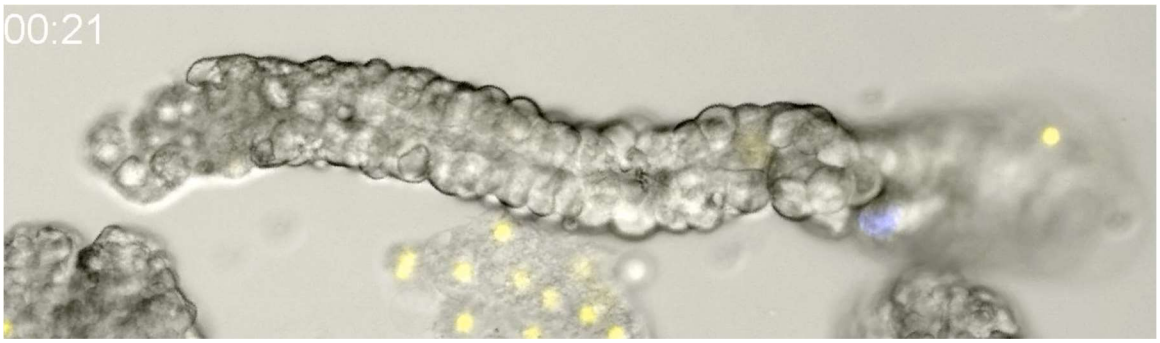

Video S4. Spontaneous necrosis of freshly isolated tubules from male mouse stained with BiotrackerTM 609 Red Ca^{2+} AM dye (pseudo-colored in blue) and SYTOX green (pseudo-colored in yellow).

Video S5. Spontaneous necrosis of freshly isolated tubules from male mouse stained with MitoTracker® Red FM (pseudo-colored in blue) and SYTOX green (pseudo-colored in yellow).

Supplementary Files

This is a list of supplementary files associated with this preprint. Click to download.

- SIvideo1femalemaleannotation.mp4
- SIvideo2outgrowth.mp4
- SIvideo3wave.mp4
- SIvideo4waveCa2.mp4
- SIvideo5mitotracker.mp4